ASTROBIOLOGY
Volume 21, Number 11, 2021
Mary Ann Liebert, Inc.
DOI: 10.1089/ast.2020.2431

The Molecular Record of Metabolic Activity in the Subsurface of the Río Tinto Mars Analog

David C. Fernández-Remolar,[1,2] David Gomez-Ortiz,[3] Ting Huang,[1,2] Angélica Anglés,[1,2] Yan Shen,[1,2] Qitao Hu,[1,2] Ricardo Amils,[4,5] Nuria Rodríguez,[4] Cristina Escudero,[4] and Neil R. Banerjee[6,7]

Abstract

In the subsurface, the interplay between microbial communities and the surrounding mineral substrate, potentially used as an energy source, results in different mineralized structures. The molecular composition of such structures can record and preserve information about the metabolic pathways that have produced them. To characterize the molecular composition of the subsurface biosphere, we have analyzed some core samples by time-of-flight secondary ion mass spectrometry (ToF-SIMS) that were collected in the borehole BH8 during the operations of the Mars Analog and Technology Experiment (MARTE) project. The molecular analysis at a micron-scale mapped the occurrence of several inorganic complexes bearing PO_3^-, $SO_{x(2\ to\ 4)}^-$, $NO_{x(2,3)}^-$, $FeO_{x(1,2)}^-$, SiO_2^-, and Cl^-. Their distribution correlates with organic molecules that were tentatively assigned to saturated and monounsaturated fatty acids, polyunsaturated fatty acids, saccharides, phospholipids, sphingolipids, and potential peptide fragments. SO_x^- appear to be mineralizing some microstructures larger than 25 microns, which have branched morphologies, and that source SO_3-bearing adducts. PO_3-rich compounds occur in two different groups of microstructures which size, morphology, and composition are different. While a group of >40-micron sized circular micronodules lacks organic compounds, an ovoidal microstructure is associated with *m/z* of other lipids. The NO_2^-/NO_3^- and Cl^- ions occur as small microstructure clusters (<20 microns), but their distribution is dissimilar to the mineralized microstructures bearing PO_3^-, and SO_3^-. However, they have a higher density in areas with more significant enrichment in iron oxides that are traced by different Fe-bearing anions like FeO_2^-. The distribution of the organic and inorganic negative ions, which we suggest, resulted from the preservation of at least three microbial consortia (PO_4^--, and NO_2^--/NO_3^--mineralizers PO_4-lipid bearing microstructures), would have resulted from different metabolic and preservation pathways. Key Words: Underground—Microbial communities—Preservation—Biomineralization—Extreme analogs. Astrobiology 21, 1387–1405.

1. Introduction

The emergence of the terrestrial biosphere was propelled by the preexistence of geochemical cycles that likely were the original core of nascent metabolic pathways (Nealson and Rye, 2014). They probably involved early stages of energy transduction in prebiotic processes, which were inherited by the oldest microbial communities on Earth. Such processes have tied the evolving microbial communities to several different geochemical cycles occurring on Earth for more than 3.5 billion years, which have induced a strong imprint on Earth's mineral composition (Hazen *et al.,* 2008; Hazen 2012). This is indeed observed in the underground communities where energy as well as CO_2 and N_2 fixation

[1]SKL Lunar and Planetary Sciences, Macau University of Science and Technology, Taipa, SAR China.
[2]CNSA Macau Center for Space Exploration and Science, Macau, PR China.
[3]ESCET-Área de Geología, Universidad Rey Juan Carlos, Móstoles, Madrid, Spain.
[4]Centro de Astrobiología (INTA-CSIC), Torrejón de Ardoz, Spain.
[5]Centro de Biología Molecular Severo Ochoa (CSIC-UAM), Universidad Autónoma de Madrid, Madrid, Spain.
[6]Department of Earth Sciences, Faculty of Science, University of Western Ontario, London, Ontario, Canada.
[7]Institute for Earth and Space Exploration, University of Western Ontario, London, Ontario, Canada.

comes from the interplay with the mineral realm. From such interplay, subsurface microbial life not only obtains energy by uptaking inorganic compounds for its development but also has a strong impact on the geochemical composition of Earth's crust (Brantley *et al.,* 2012; Lyons *et al.,* 2014). If the geosphere has recorded unequivocal evidence of ancient biological activity, the geobiologist can reconstruct the ancient metabolic pathways through one of the fundamental basic pillars of geology which is the actualism. For such an approach, the researcher has a wide set of analytic instruments available whose use is essential to understand how the preservation processes have operated and which metabolic activity was involved in the alteration of Earth's crust.

In this paper, we show the geobiological record of ancient microbial metabolisms that have been involved in a complex interplay with the sulfide-rich Río Tinto Mars analog basement over the last 25 million years (Essalhi *et al.,* 2011). Although this has been the main aim in several other papers (Fernández-Remolar *et al.,* 2008, 2018), our recent research provides novel data obtained from the sample analysis by using state-of-the-art ToF-SIMS (time-of-flight secondary ion mass spectrometer) technology. It has also been supported by conventional imaging and geochemical techniques, which were the primary source of data in previous refereed works. As ToF-SIMS provides the compositional mapping of biological and nonbiological compounds at the microscale, it is possible to ascertain a direct relation between fabric and microstructures with biotic and nonbiotic by-products (Fernández-Remolar *et al.,* 2015). As a result, we can trace direct association between microstructures and different inorganic (*e.g.,* NO_2^-/NO_3^-, PO_4^-, HS^-, SO_4^-) and biomolecular ions supporting a biological origin, *in situ*. Indeed, it is possible with our techniques to recognize a specific group of structures that are strictly associated with the mineralization of N-bearing anions, which provide essential information about the nitrogen cycle in the subsurface.

The results are relevant to a much broader framework, where the same techniques and procedures can be applied to understand how the different metabolic paths sustaining biogeochemical cycles have been operating in the subsurface on the long-term temporal scale, as well as how they could potentially be identified on other planetary bodies to demonstrate the emergence of non-terrestrial biospheres in the Solar System. This will come together with the careful analysis of materials from sample return missions, which will play an essential role in understanding whether life has arisen in other regions of the Universe.

2. Geological Settings

The geological record of ancient metabolism operating in the subsurface has been sampled through drilling the Río Tinto basement in the Peña de Hierro area (Fig. 1A). It is located in the Iberian Pyrite Belt (IPB), a 250 km long and 60 km wide unit of volcanogenic massive sulfide deposits that belong to the South Portuguese Zone, the southernmost terrane of the Variscan Belt of Iberia (Fig. 1B). Several geological units comprise the IPB; however, except for its late- to post-Variscan intrusive rocks and continental intermontane deposits, three different units define its general lithostratigraphy: the Phyllite-Quartzite (PQ) unit at the bottom, the intermediate Volcanic Sedimentary Complex (VSC) unit with massive and stockwork sulfides, and the Culm Group at the top. In the Río Tinto area, the sulfide bio-oxidation has led to the formation of a gossan reaching up to 10 m depth which formation has occurred in three different alteration episodes averaging 25, 7, and 2 Ma (Essalhi *et al.,* 2011; Velasco *et al.,* 2013).

During the last 20 years, extensive exploration of the geological, geophysical, and microbiological conditions in the Río Tinto area, especially in Peña de Hierro, has provided a huge amount of data about both the surface and subsurface geology of the area (Fernández-Remolar *et al.,* 2005, 2008; Gómez-Ortiz *et al.,* 2014). The data comprises geophysical information and several boreholes (BH1, BH4, BH8, BH10, and BH11) ranging from 59 to 610 m depth, which has provided lithological information about the subsurface structure around the Peña de Hierro orebody (Fernández-Remolar *et al.,* 2018).

Sample BH8-24c was collected at a depth of around 40 m along a 165 m deep borehole collared 50 m east of Peña de Hierro pit lake (Fig. 1A). It occurs north of the San Miguel-Minas del Castillo Shear Zone, mainly composed of shales, acidic tuffs, and volcanic materials (Fig. 1A). The upper unit is composed of 25.5 m thick orange acidic tuffs (Fig. 1A) affected by low-grade metamorphism. The acidic tuff unit is followed by an intermediate unit ranging from a 25.5 to 31 m thickness consisting of a gossan deposit with chert. In this zone, the characteristics of the gossan do not correspond to the oxidization of massive sulfides but hematite and goethite-rich gossanized tuffs. The mineralogical distribution of the gossan (Fernández-Remolar *et al.,* 2008) agrees with the general vertical gossan profile previously defined. The upper part of the gossan is dominated by hematite and quartz with minor amounts of goethite. In contrast, at the bottom, the goethite is a dominant mineral together with quartz, where hematite is secondary.

The lower unit consists of a pyritic stockwork extending from 31 m depth to the bottom of the borehole. It is mainly composed of quartz and pyrite with lower contents of barite, feldspars, chlorite, mica, and siderite (Fernández-Remolar *et al.,* 2008, 2018). The upper part ($\sim$12 m), where sample BH8-24c was collected, shows iron oxides replacing pyrite associated with quartz veins. The rest of the unit is an unaltered stockwork excepting two slightly oxidized horizons extending from 66 to 92 m depth and 103.5 to 109 m depth. At the borehole bottom (151 to 166 m depth), the stockwork is affected by small (millimeter- to centimeter-sized) fractures filled by secondary sulfates, iron oxides, and chlorite.

3. Methods

3.1. Sample collection and preparation

As discussed above, core samples were collected at a depth of 40 m during the Mars Analog and Technology Experiment (MARTE) project drilling operations that were arranged to research the traces of the microbial communities living in the IPB basement. The procedures for sampling and preparing underground materials are described in detail elsewhere (Fernández-Remolar *et al.,* 2008, 2018; Stoker *et al.,* 2008) and will not be described in detail in this paper. In short, subsurface sample collection was performed with a Boart-Longyear (Salt Lake City, UT, USA) HQ wireline system that produced 60 mm diameter cores within a plastic liner. A chemical tracer (NaBr) was added into the drilling

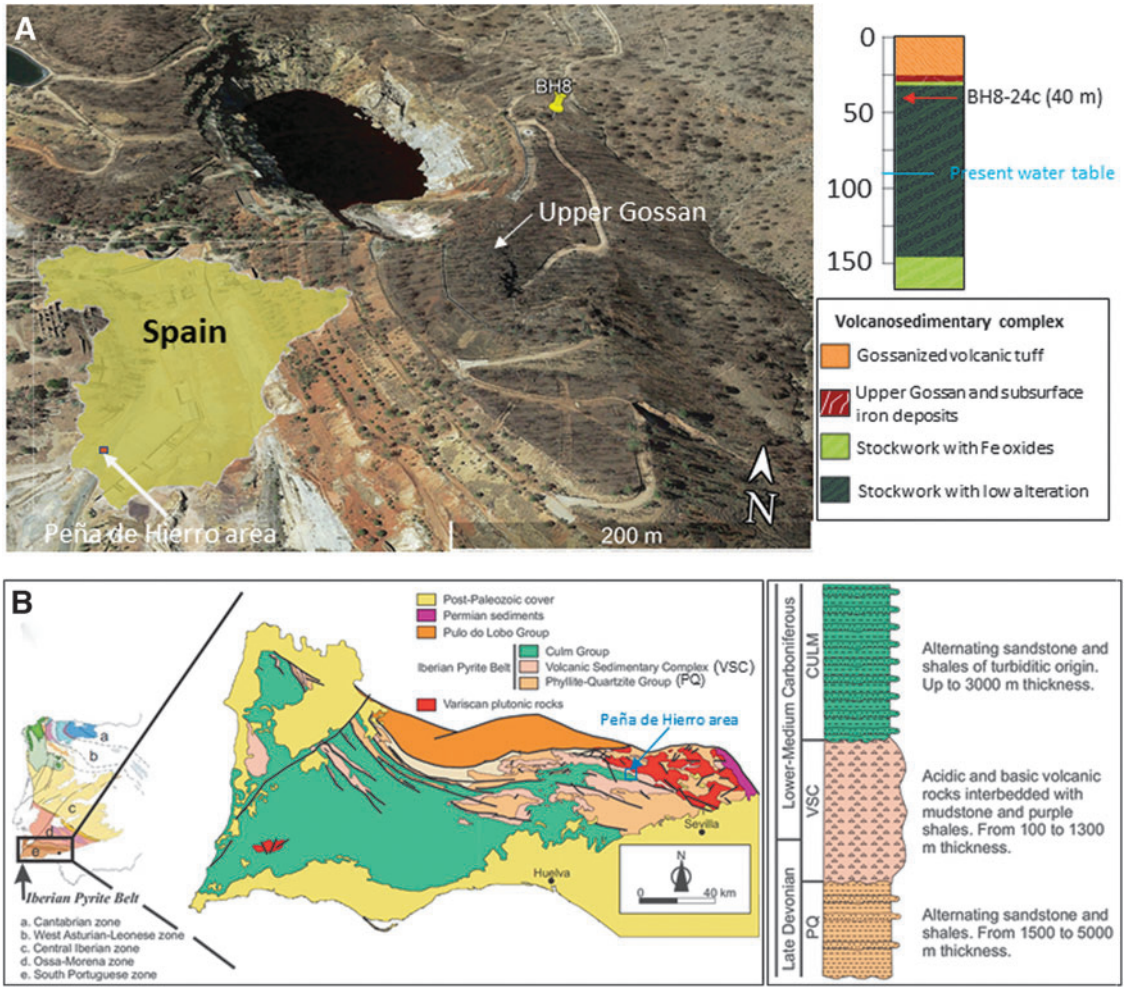

FIG. 1. Composite image showing (**A**) the occurrence of the hydrothermal and gossan deposits drilled in the borehole BH8, which lithology is displayed in the stratigraphic column, and (**B**) the geological situation of the Carboniferous materials containing the igneous materials in Peña de Hierro. CULM = the Culm Group; PQ = Phyllite-Quartzite unit; VSC = Volcanic Sedimentary Complex unit.

fluid to identify possible sample contamination during the drilling process. Core providing sample BH8-24c had no bromide traces in the interior, which evidences that it was not contaminated with the drilling fluid. Cores were retrieved in 1 m sections encased in plastic liners. These liners were flushed with N_2 gas at the borehole, sealed, and then transported to a field laboratory within 1 h, approximately 6 km from the borehole.

The core was split into several subsamples and cut with a pneumatic rock cutter and a diamond saw blade. Thin sectioning was prepared through cutting and polishing a subsample set by using a 0.3 micron-sized alumina paste for both transmitted light microscope inspection and ToF-SIMS surface analysis. A second subsample set was split into small fragments (<1 cm) to expose fresh material to search for traces of microbial activity under a scanning electron microscope (SEM).

3.2. Light microscope and scanning electron microscope

Samples were scrutinized under both light microscope and SEM to find secondary ferruginous deposits mineralizing microbial structures or other mineral traces that could have resulted from ancient microbial activity. Thin sections were observed under a Leica stereomicroscope and an upright trinocular microscope Motic BA400 coupled to a MoticamPro 282a camera. Thin section examination was complemented with SEM analysis. For such purpose, the rock sample was coated with gold by way of an SC7620 Thermo VG Scientific sputter-coating device. Semiquantitative chemical image microanalysis was done under a JEOL JSM-5600V scanning electron microscope coupled to an Oxford INCA X-sight EDS (energy dispersive X-ray spectroscopy) Microanalysis Probe, which are emplaced in the Center of Astrobiology in Madrid.

3.3. Time-of-flight secondary ionization mass spectrometry analysis

Before analysis, thin sections were cleaned by surface sputtering with a 100 nA 3V oxygen ion beam for 3 s over a square area of 500 × 500 μm. The ToF-SIMS analyses were performed with a ToF-SIMS IV (ION-TOF, Münster, Germany) that was emplaced at the Nanotechnology Platform, Institute for Bioengineering of Catalonia in Barcelona.

Under an operational pressure of 5×10^{-9} mbar, the sample was bombarded with a pulsed bismuth liquid metal ion source (Bi_3^{++}), at energy of 25 keV. The gun was operated with a 20 ns pulse width, 0.3 pA pulsed ion current for a dosage lower than 5×10^{11} ions/cm^2, well below the threshold level of 1×10^{13} ions/cm^2 generally accepted for static SIMS conditions.

Secondary ions were detected with a reflector time-of-flight analyzer, a multichannel plate, and a time-to-digital converter. Charge neutralization was achieved with a low-energy (20 eV) electron flood gun. Secondary ion spectra were acquired from randomly rastered surface areas of 500×500 µm within the sample's surface. Secondary ions were extracted with 2 kV accelerating voltage and were postaccelerated to 10 keV kinetic energy before hitting the detector. Mass spectral acquisition and image analysis were performed within the ION-TOF Ion Spec and Ion image software (version 7.4).

Spectral analysis and molecular identification were assisted by the software Mmass (Strohalm *et al.,* 2010) and the molecular database Metlin (Smith *et al.,* 2005). Data calibration used different known inorganic anions (*e.g.,* Cl^-, SO_2^-, PO_3^-) that provided an accuracy of <90 ppm, which is sufficient in terms of ToF-SIMS analysis (Sjövall *et al.,* 2008).

4. Results

4.1. Transmitted light microscope and scanning electron microscope

Visual inspection led to selecting a few core samples showing clear evidence of rock alteration and ferric mineralization in millimeter-sized cracks or microcavities left by pyrite dissolution. This is the case for samples BH8-22b, BH8-23c, BH8-24c, and BH8-25c occurring between 34 and 43 m below the surface. They consist of a weathered stockwork composed of cherty mass crosscut by sulfide-rich veins and cracks, which have been attacked, dissolved, and infilled with iron oxides (Fig. 2A, 2B) (Fernández-Remolar *et al.,* 2008). The ferruginous infill consists of glassy iron oxide occurring as a massive cavity infill or several micron-scale thin laminae stacks growing at both crack faces. In some cases, the laminae stacks grow toward the crack or cavity interior to coalesce and form a unique deposit (Fig. 2B). Such laminations contain aggregates of dark particles and <1 micron thickness and up to 100 micron length isolated filaments with straight to curvilinear outline (Fig. 2C, 2D).

SEM imaging of sample BH8-24c showed an abundance of filament structures that flourished, embedding the upper part of the lamination surface (Fig. 2C) with nanometer-scale mineralized particles (Fig. 2D). A comparative elemental analysis of the filamentous structures and the lamination surface through the energy dispersive X-ray spectroscopy (EDS) microanalysis system show that the N content in filaments ($\sim$9 atomic %) doubles the N concentration in the lamina surface (Fig. 2E). In addition, both filamentous structures and laminae have a high enrichment in C ($\sim$18 atomic %), which concentration is higher than Fe ($\sim$12 atomic %).

The filament and lamination EDS analysis show a secondary concentration in Si and a minor concentration in S averaging 3 and 0.7 atomic %, respectively. The occurrence of C and Fe as major, Si as secondary, and S as minor elements suggests that the mineral matrix of the cracks and microcavity ferric infillings were initially composed of ferric oxysulfates that have experienced dehydration and sulfate loss during diagenesis (Fernández-Remolar *et al.,* 2011). Furthermore, the occurrence of Si as a secondary element suggests that it plays a role in the mineralization and preservation of the biological remains in the Río Tinto materials (Fernández-Remolar and Knoll, 2008).

4.2. Time-of-flight secondary ion mass spectrometry analysis

The ToF-SIMS analysis has performed molecular mapping and spectral analysis of negative ions in sample BH8-24c. The target area was selected to have different structures of potential biological origin found inside the laminated ferruginous deposits that are infilling cracks and microcavities (Fig. 2C, 2D). The molecular mapping of positive and negative masses establishes a direct association between molecular composition and structure. At the same time, the spectral analysis provides additional information about the molecular composition recorded in the sample. The combination of physical properties and composition is essential to ascertain biogenicity in the preserved microstructures (Cady *et al.,* 2003; Westall *et al.,* 2015).

As the ToF-SIMS analysis provides direct information about the relation between the preserved biological structures and the mineral substrate, it is a reliable tool to distinguish mineralization from ancient metabolic activity in the Río Tinto subsurface (Fernández-Remolar *et al.,* 2018).

4.2.1. Image analysis. The ToF-SIMS molecular mapping targeted a 500×500 micron sized area with ferruginous laminations occurring as crack fillings (Fig. 3). As a result, the more abundant fragment ions outline three main image patterns (Fig. 4), which are the following

Group 1 is defined by the distribution of major negative ions, including CN^-, CON^-, HS^-, and CNP^- (Fig. 4A). The same fragment distribution is also found in different major N-bearing negative ions like $C_2H_2N^-$ and $C_3HN_2^-$. Although the pattern is mostly homogeneous, in some locations of the images (bottom left), the ion intensity decreases to follow a layered fabric or increases to develop a branched filamentous structure (Fig. 4A). The occurrence of those set of ions bearing C, P, O, and N has been associated with the fragmentation of amino acids and peptidic chains (Kawecki and Bernard, 2018), which have also been found in the ancient fluvial deposits of Río Tinto dating back to 2.1 Ma (Colín-García *et al.,* 2011). Such ion distribution is also observed in the plot showing the image addition of several negative masses to enhance the total signal intensity. Such negative masses were found at 47.00, 50.01, 56.99, 65.01, 66.00, 72.01, 74.00, 85.03, 85.98, 86.02, 89.05, 98.02, 112.02, and 113.05 (see Fig. 4A1), which fits *m/z* ions like CH_3S^-, C_3N^-, C_2HS^-, $C_3HN_2^-$, C_3NO^-, $C_2H_2NO_2^-$, $C_2H_4NS^-$, $C_3H_3N_3^-$, $C_4H_5O_2^-$, CSN_3^-, $C_3H_4NO_2^-$, $C_3H_7NO_4^-$, $C_4H_4NO_2^-$, $C_4H_4N_2O_2^-$, and $C_5H_7NO_2^-$. Although some of those masses have also been identified as negative ions sourced from amino acid fragmentation (Kawecki and Bernard, 2018), they could also be produced by the ionization of different N-bearing molecular compounds like lipids.

Group 2 outlines the lamination fabric which intensity increases from the upper right to the lower left corner in the analyzed area (Fig. 4B). It is mainly defined by three *m/z*

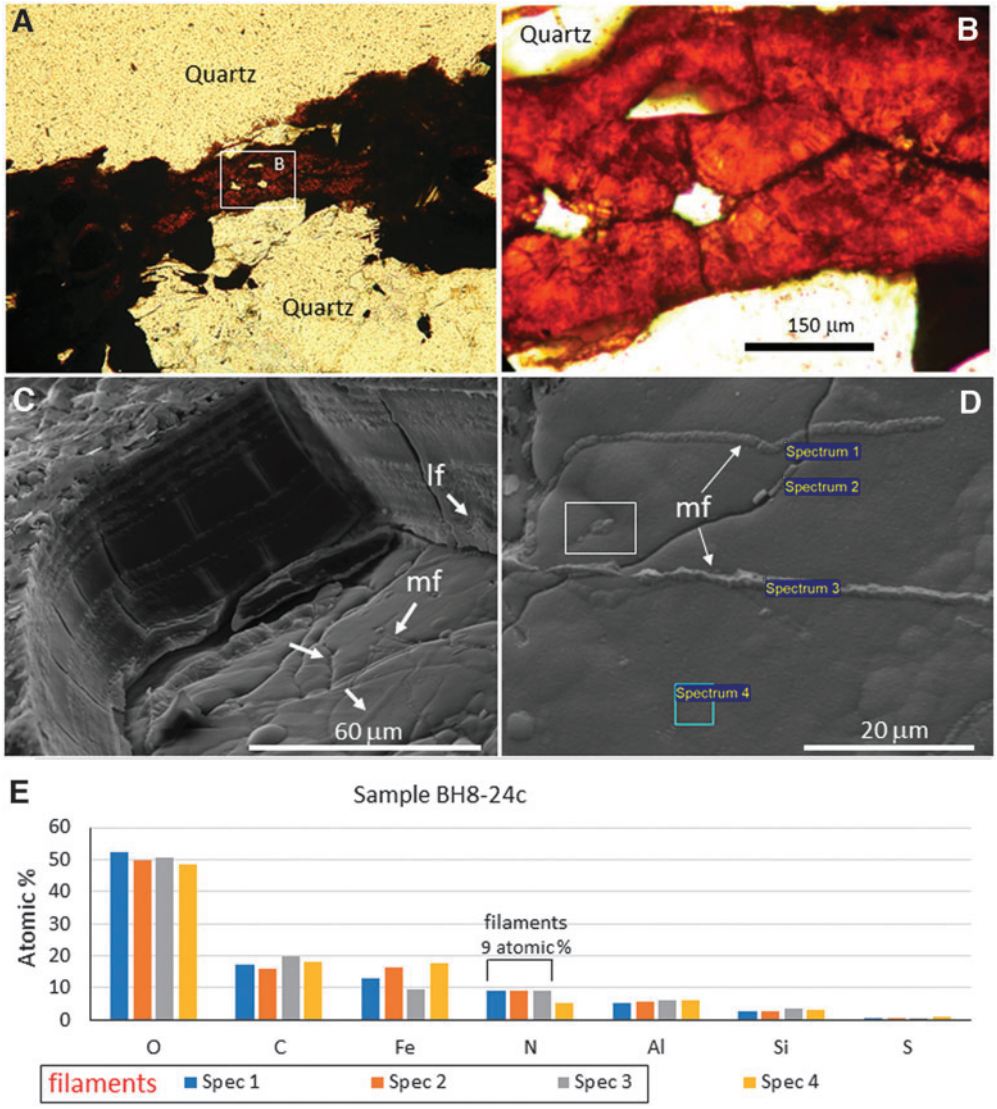

FIG. 2. Microscope images showing different aspects of ferruginous laminations infilling the stockwork deposits in sample BH8-24c at a depth of ~40 m. Panels (**A**) and (**B**) correspond to light microscope pictures of a ferruginous laminar deposit infilling a crack formed inside the orebody stockwork. Panels (**C**) and (**D**) are SEM images showing different microstructures like macrofilaments (lf) and microfilaments (mf) that develop on the lamination surface. The microfilaments usually occur entrenched on the lamination surface and eventually are filled (D) by small bodies (<0.5 microns). EDS analysis (**E**) of microfilaments (spec 1 to spec 3) and lamination surface (spec 4) show a high N enrichment in the microfilaments; the occurrence of Si suggests pH changes at microscale.

peaks found at 27.97, 59.97, and 75.97 that fit anions like Si^-, SiO_2^-, and $Si_2H_4O^-$, respectively (Supplementary Table S1). Although most inorganic negative ions follow an inverse distribution defined in Group 3, the Cl-, S-, and N-bearing anions also co-occur with the silica anions suggesting that the mineralizing process produces mixtures of secondary inorganic compounds as has been observed through the SEM-EDS analysis (Fig. 2C–2E).

Group 3 is characterized by various negative ions outlining the lamination fabric but following a molecular intensity inverse to Group 2. Such a pattern is followed by a different set of negative ions that show slight pattern variations as (see Fig. 4C1–4C8): (1) CNP^-; (2) COP^-; (3) Cl^- (34.97); (4) 96.97 (HSO_4^-), 265.14 ($C_{12}H_{25}SO_4^-$), and 279.16 ($C_{13}H_{27}SO_4^-$); (5) FeO^-, FeO_2^-, and $Fe_2H_5O_2^-$; (6) 45.99 (NO_2^-) and 61.99 (NO_3^-); (7) 78.96 (PO_3^-); and (8) CHO_2^-. In this regard, the intensity distribution of ion sets like PO_3^-/$C_{38}H_{73}NO_6P^-$, NO_2^-/NO_3^-, and SO_3^-/$C_{12}H_{25}SO_4^-$/$C_{13}H_{27}SO_4^-$ show higher intensities as round-shaped microstructures, which reveals higher mineralization or enrichment in those compounds (Fig. 5A). Although they usually are 20–25 microns in size (*e.g.,* P- and S-bearing ions), this is not the case for the NO_x-bearing anions that are materialized as smaller (<10 µm) and abundant micronodules in the sample (Fig. 4C4). The size of N-bearing micronodules meets the thickness of N-enriched filamentous structures detected by SEM-EDS. Interestingly, the Cl^- occurrence partly meets the NO_2^- and NO_3^- distribution, suggesting that it could be associated with similar processes leading to the nitrogen accumulation in the preserved microstructures.

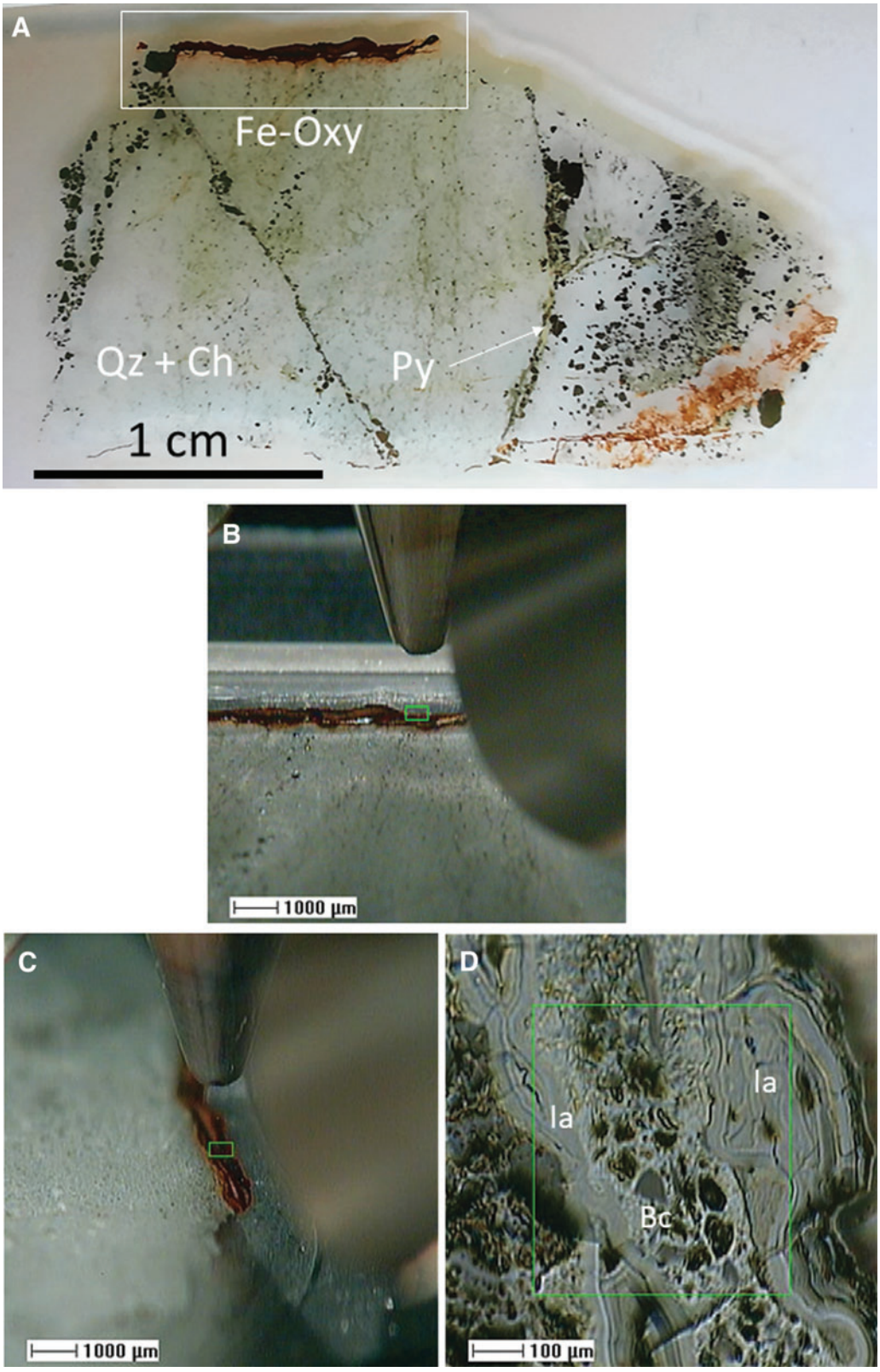

FIG. 3. Mosaic of images of sample BH8-24c including a thin section picture **(A)** showing the geometry of the ferruginous lamination (Fe-Oxy), infilling a quartzic and chloritic matrix (Qz + Ch) with disseminated pyrite (Py); and from two different target areas TA **(B)** and TB **(C)** obtained by the visible camera integrated in the ToF-SIMS. It shows the same ferruginous deposits infilling a crack in the silica-rich stockwork deposit. **(D)** ToF-SIMS SEM image showing a higher detail of the microstructure in TB where it can be recognized as a brecciated (Bc) texture that alternates with two fine-laminated layers (la).

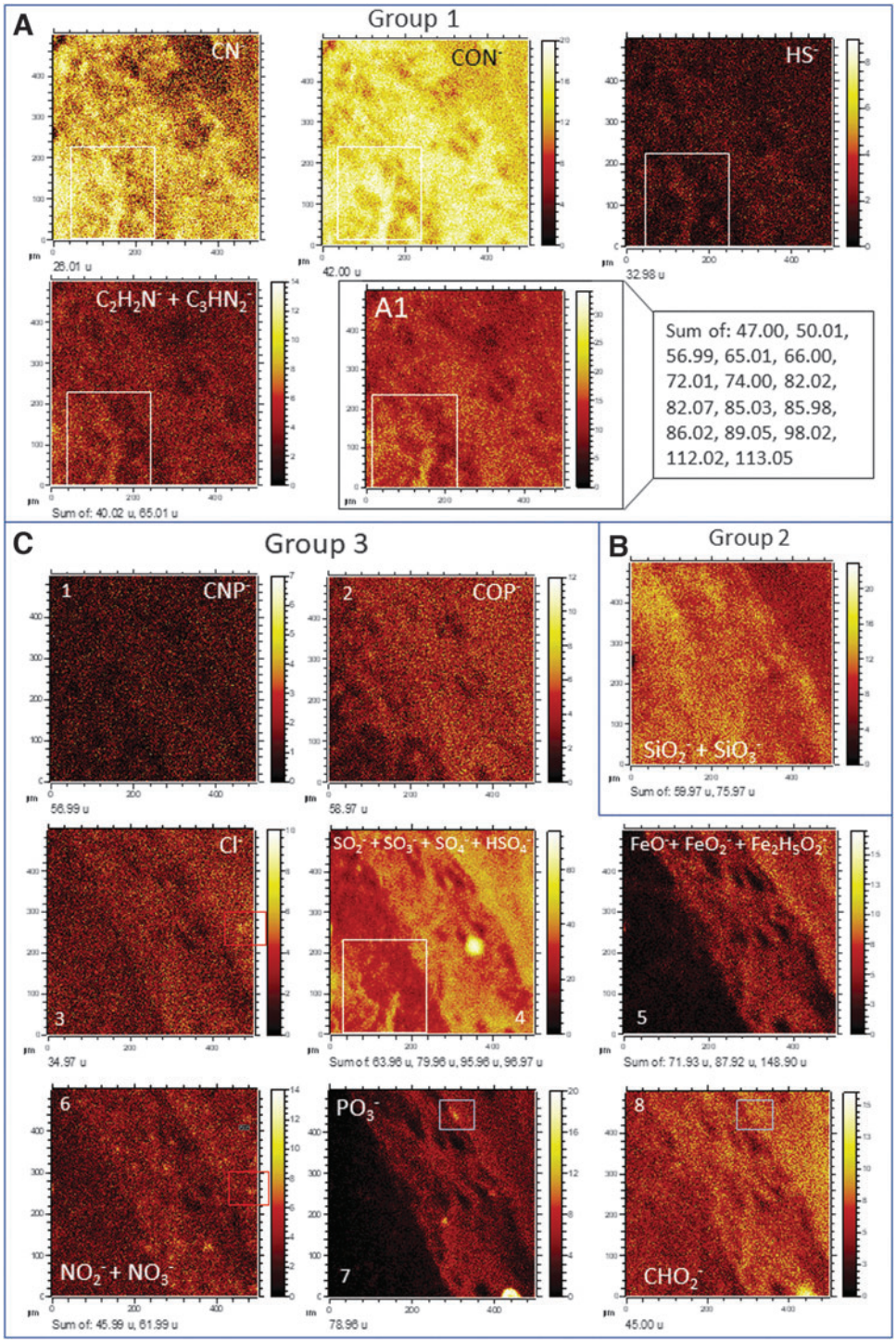

FIG. 4. ToF-SIMS mapping of different anions obtained in the target area TA (Fig. 3A, B), which outline can be classified into three different main patterns. (**A**) Group 1 defined by branched microstructures at the left bottom with minor pattern changes: as CN^-, CON^-, and N-bearing ions (see A1) showing a higher intensity at the middle and left of the target area, CNP^- with a more homogeneous distribution, and COP^- with a higher intensity at the middle and right. (**B**) Group 2 shows the silica distribution, which follows the lamination fabric and increases the intensity at the left of the image. (**C**) Group 3 follows the Fe-bearing mineral lamination with minor pattern variations like CNP^- (1), COP^- (2), Cl^- (3), intensity sum of S-inorganic anions (4), intensity sum of Fe-inorganic ions (5), intensity sum of NO_2^- and NO_3^- (6), PO_3^- (7), and CHO_2^- (8). They follow the main lamination orientation but inversely to Group 2. The white square delimits a branched filamentous structure in Groups 1 and 3; the red square points to a nodule where Cl^-, NO_2^-, and NO_3^- concur with a high intensity; and the blue square spots the PO_4-rich nodule sourced in lipids. The image shown in A1 has been defined by the sum of the *m/z* fragments at 47.00, 50.01, 56.99, 65.01, 66.00, 72.01, 74.00, 85.03, 85.98, 86.02, 89.05, 98.02, 112.02, and 113.05, which fits CH_3S^-, C_3N^-, C_2HS^-, $C_3HN_2^-$, C_3NO^-, $C_2H_2NO_2^-$, $C_2H_4NS^-$, $C_3H_3N_3^-$, $C_4H_5O_2^-$, CSN_3^-, $C_3H_4NO_2^-$, $C_3H_7NO_4^-$, $C_4H_4NO_2^-$, $C_4H_4N_2O_2^-$, $C_5H_7NO_2^-$, and $C_5H_7NO_2^-$. Some of those anions are found in the fragmentation series of some amino acids (Kawecki and Bernard, 2018).

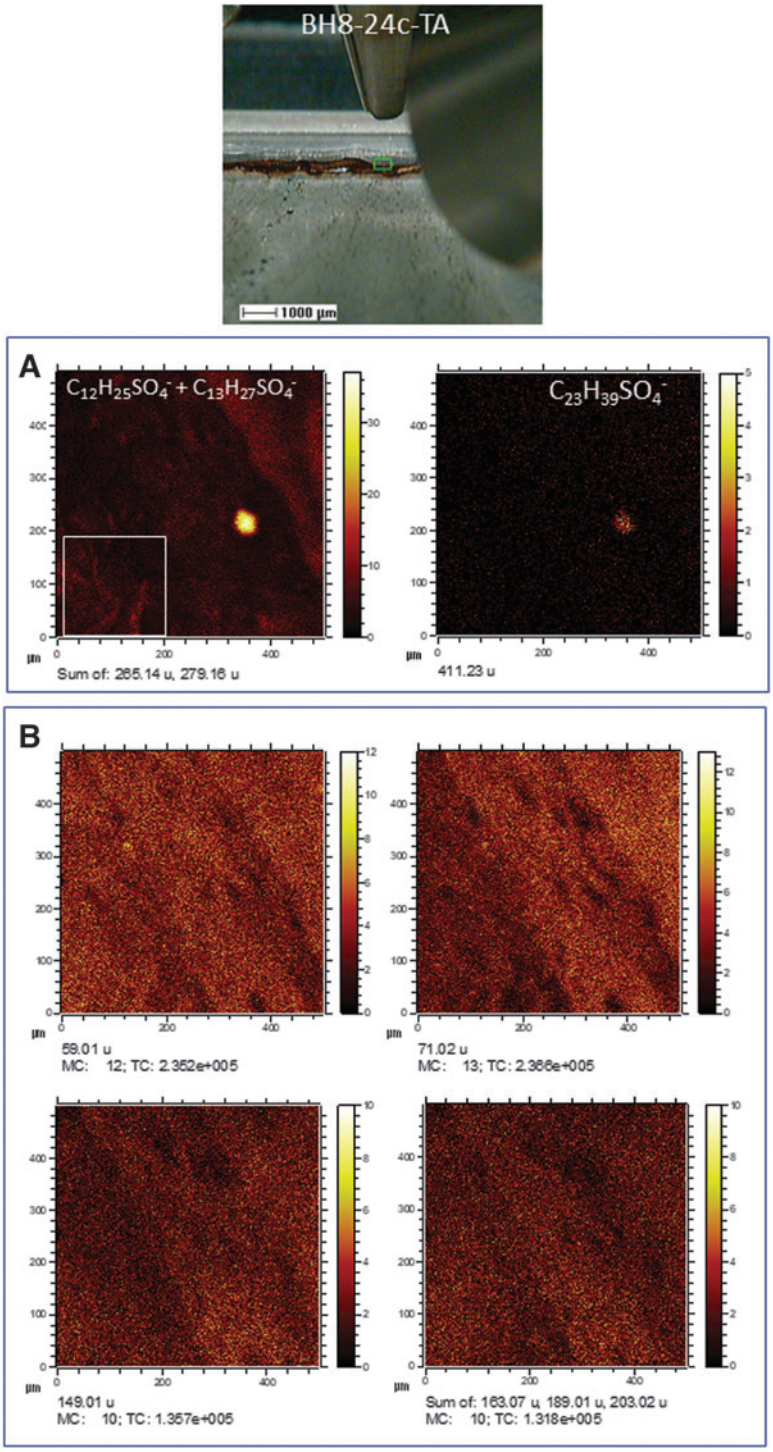

FIG. 5. Mosaic of different ToF-SIMS ion images obtained from target area TA. (**A**) ToF-SIMS image of SO_4-bearing organic anions following the pattern defining Group 3. They could come from the mineralization of an organic layer by a fluid enriched in sulfates. The white square traces the same branched filamentous structure shown in Fig. 4. (**B**) ToF-SIMS image of the occurrence of *m/z* 59.01, 71.02, 149.01, 163.07, 189.00, and 203.01, tentatively assigned to saccharide fragments like $C_2H_3O_2^-$, $C_3H_3O_2^-$, $C_4H_5O_6^-$, $C_6H_{11}O_5^-$, $C_6H_5O_7^-$, and $C_7H_7O_7^-$. The anion distribution is very similar, supporting a common origin for them.

4.2.2. Spectral analysis. The fragmentation pattern of the negative ions found in sample BH8-24c has provided the detection of different major groups of organic compounds and biomolecules, which can eventually be mapped (Figs. 5 and 6)

Sulfate adducts (SA). High intensity *m/z* peaks found at 207.06, 265.14, 279.16, 293.17, and 411.24 fit well negative SA like $C_8H_{15}SO_4^-$, $C_{12}H_{25}SO_4^-$, $C_{13}H_{27}SO_4^-$, $C_{14}H_{29}SO_4^-$, and $C_{23}H_{39}SO_4^-$, respectively. The SA distribution in the mapping area (Fig. 5A) is strictly associated with the outline pattern of the different SO_x^- anions that have defined Group 3 (Figs. 4C and 5A). Although the origin of the SA is unknown, we suggest it comes from the formation of oxyl or ester bonds between SO_2^- or SO_3^- and lipids with alcohol and carboxylic groups that have been sputtered from the same area by the ion beam. Therefore, its formation traces the mineralization over an organic template by an overconcentrated solution in sulfate that has been sourced in the biooxidation of the subsurface sulfide orebody (Fernández-Remolar *et al.,* 2018).

Fatty acids (FAs). The spectral analysis shows that FAs have a great variety (Fig. 6A; Supplementary Table S1),

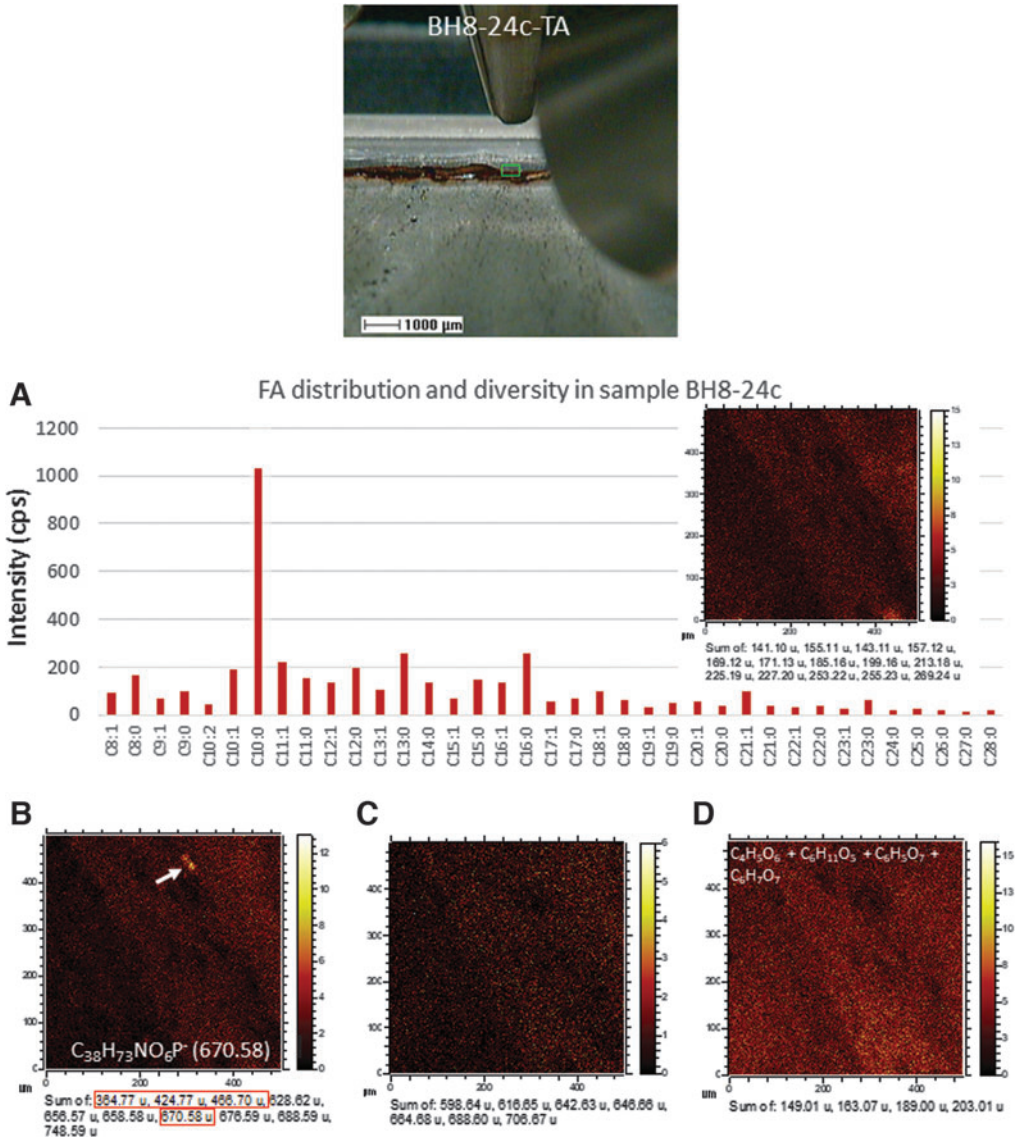

FIG. 6. (**A**) Bar diagram plotting the mass distribution of saturated and monounsaturated fatty acids (FAs). ToF-SIMS images show the intensity distribution of an intensity sum of saturated and monounsaturated FAs ($C_{14:0}$, $C_{15:0}$, $C_{16:1}$, and $C_{16:0}$), which show a distribution akin to Group 3. Combination of different ToF-SIMS mapping images showing the distribution of anions recording mineral, biomolecular, and metabolic information. (**B**) The image results from the intensity sum of varying *m/z* fragments meeting major glycerophospholipid masses; this is supported by the presence of the PO_4-rich nodular structure (white square) seen in Fig. 4C5. (**C**) Sum of $[M - H_2O - H]^-$ and $[M - H]^-$ sphingolipid anions showing an intensity pattern meeting the molecular distribution in Group 3. (**D**) Sum of four negative fragments of saccharides which intensity distribution follows the lamination orientation. The ToF-SIMS ion images were collected from the target area TA.

including unsaturated and monounsaturated chains. The detection of *m/z* peaks assigned to FAs currently ranges from $C_{8:1}$ and $C_{8:0}$ to $C_{28:0}$. The distribution diagram plotting $[M - H]^-$ unsaturated and saturated FAs (Fig. 6) shows that the peak intensity is higher in *m/z* fragments (Supplementary Table S1) whose mass is equal to or smaller than 267.24 ($C_{17:1}$), where reaches a maximum at $C_{16:0}$. The total FA amount resulting by adding the $[M - H]^-$ ion intensity (Fig. 6) shows that the saturated and monounsaturated $\leq n$-C_{20} fatty acids have a higher intensity than the $> n$-C_{20} fatty acids. In contrast, the total intensity of even exceeds odd in $\leq n$-C_{20} chains as well. Such distribution is consistent with a short-chained and even-over-odd FA predominance, suggesting that the production of FAs in the subsurface is driven by a microbial community dominated by bacteria (Harwood and Russell, 1984; Killops and Killops, 2005).

The ToF-SIMS mapping in sample BH8-24c shows that the FA distribution fairly outlines the main lamination orientation following the pattern found in Group 3 (Fig. 6), where the intensity decreases as the S- and Fe-bearing inorganic ions do (Fig. 4C). However, FAs are also occurring in areas with higher content in SiO_2^- and $Si_2H_4O^-$ that is consistent with preservation with mineralization with silica.

Large fragment lipids (> 600 Da). Different even negative peaks are found in the analyzed area, some of which follow distribution of the PO_4^- anions (*e.g.,* Fig. 6B and 6C;

Supplementary Fig. S1). Although the fragmentation pattern has not been analyzed in detail, the spectral data show some features as a 14 Da peak separation characteristic of lipids. The characterization of the molecular sum suggests that they come from at least two different groups of compounds (Supplementary Fig. S1; Supplementary Table S1) as the following:

(1) Compounds larger than 600 Da which sum has been defined through the Metlin database (Smith *et al.,* 2005) as $C_{37}H_{71}NO_6P^-$ (656.57), $C_{37}H_{73}NO_6P^-$ (658.58), $C_{38}H_{73}NO_6P^-$ (670.58), $C_{38}H_{79}NO_6P^-$ (676.59), and $C_{44}H_{79}NO_6P^-$ (748.59), $C_{40}H_{69}NO_{10}P^-$ (754.43), $C_{40}H_{71}NO_{10}P^-$ (756.42), and $C_{40}H_{75}NO_{10}P^-$ (760.40). Although the compound distribution follows the pattern shown in Group 3 (Fig. 4C), they show a higher intensity outlining the PO_4-bearing micronodule (Fig. 6B). Such composition is similar in the mass range to some bacterial phospholipids characterized by ToF-SIMS and other mass spectrometry techniques (Mazzella *et al.,* 2005; Heim *et al.,* 2009; Bühring *et al.,* 2012). The ToF-SIMS mapping of the compounds listed above shows the same distribution as the pattern, followed by a set of unknown anions including 364.77, 424.77, 466.70, 568.65, and 628.62 (Fig. 6B), which could be related to adducts of phosphates.

(2) A set of different even negative fragments fitting N-bearing compounds (Fig. 6C; Supplementary Fig. S1; Table S1) that can tentatively be assigned as $C_{42}H_{82}NO^-$ (616.63), $C_{42}H_{78}NO_2^-/C_{38}H_{79}NO_3P^-$ (628.62), $C_{42}H_{84}NO_2^-$ (634.64), $C_{43}H_{80}NO_2^-$ (642.62), $C_{43}H_{84}NO_2^-$ (646.64), $C_{43}H_{86}NO_3^-$ (664.68), $C_{45}H_{80}NO_3^-/C_{42}H_{84}NO_5^-$ (682.63), $C_{45}H_{82}NO_3^-$ (684.62), $C_{45}H_{84}NO_3^-$ (688.62), $C_{46}H_{92}NO_3^-$ (706.67), $C_{47}H_{82}NO_3^-$ (708.63), and $C_{47}H_{82}NO_4$- (724.64). They could be associated with the formation of $[M - H_2O - H]^-$ or $[M - H]^-$ ions of some ceramides (Olsen and Jantzen, 2001) as shown in the Metlin database (Smith *et al.,* 2005). The ToF-SIMS images resulting from the addition for each *m/z* (Fig. 6C) show that they distribute following the pattern of Group 3 but show a lower intensity.

The presence of the *m/z* peak at 657.53 could tentatively be assigned to $C_{42}H_{73}O_5^-$ (Supplementary Table S1), which corresponds to a diacylglyceride backbone. It could be sourced from different lipids as simple acylglycerides or phospholipids, if they come together with a polar group (Fahy *et al.,* 2005). Although the peak intensity is low, it agrees with detecting a series of abundant cations separated by 14 Da (*e.g.,* 495.44, 509.45, 523.47, 537.49, and 551.50) that evidences the presence of diacylglycerides in sample BH8-24c.

Saccharides. The mass distribution of several odd *m/z* peaks agrees with the occurrence of polysaccharide fragments like 59.01, 71.02, 149.01, 163.07, 189.00, and 203.01, which fit well $C_2H_3O_2^-$, $C_3H_3O_2^-$, $C_4H_5O_6^-$, $C_6H_{11}O_5^-$, $C_6H_5O_7^-$, and $C_7H_7O_7^-$. They are currently reported from the fragmentation of saccharolipids as acylaminosugars or glycosyl ceramides (Fahy *et al.,* 2005; Del Poeta *et al.,* 2014), though they also are a common component in extracellular polymeric substances (EPS) (Sutherland, 2001). The ion mapping resulting from the addition of anions assigned to saccharide fragments shows a homogeneous distribution in the target area following the lamination fabric (Fig. 6D). This suggests that the saccharide fragments are likely sourced in different biological compounds (*e.g.,* cell membranes, EPS) that can be abundant in the mineral subsurface substrate as biofilms (Escudero *et al.,* 2018).

Protein fragments and amino acids. Many *m/z* fragments distribute somewhat homogeneously in the target area that has been mapped with ToF-SIMS (Fig. 4A1). They correspond to a set of mostly even anions found at 47.00, 50.01, 56.99, 65.01, 66.00, 72.01, 74.00, 82.02, 82.07, 85.03, 85.98, 86.02, 89.05, 98.02, 112.02, and 113.05. The set of ions agree (Supplementary Table S2) with the occurrence of different ions like CH_3S^-, C_3N^-, C_2HS^-, $C_3HN_2^-$, C_3NO^-, $C_2H_2NO_2^-$, $C_2H_4NS^-$, $C_4H_4NO^-$, $C_5H_8N^-$, $C_4H_5O_2^-$, CSN_3^-, $C_3H_4NO_2^-$, $C_3H_7NO_2^-$, $C_4H_4NO_2^-$, $C_4H_4N_2O_2^-$, and $C_5H_7NO_2^-$, respectively, that are found in the fragmentation of amino acids (Kawecki and Bernard, 2018). The ToF-SIMS mapping of the anions listed above also meets the distribution observed by major secondary ions like CN^-, CNO^-, HS^-, CNP^-, and CPO^- (Fig. 4A), which have been reported as sourced in the fragmentation of proteins and amino acids (Siljeström *et al.,* 2017). While the N-bearing negative anions described above follow the fragmentation pattern of different amino acids, it is also possible that an amount of the total concentration of the fragment could be sourced in the ionization of other N-bearing compounds like sphingolipids, polyketides, and glycerophospholipids. However, its concentration should be low as the mapping pattern of the N-bearing ions assigned to amino acids does not follow the fabric observed in Group 3, which is outlined by the different N-bearing lipid fragments (Fig. 6C).

5. Discussion

The ToF-SIMS analysis of sample BH8-24c has combined molecular mapping and spectral analysis to recognize the mineral substrate that is the preserving matrix for biological information. It also shows the occurrence of several preserved entities that record ancient microbial activity in the form of mineralized structures. In this regard, the distribution of Fe-, S-, and Si-bearing inorganic anions, when using ToF-SIMS mapping capabilities, shows that there are three compositional areas with a characteristic mineral composition following the lamination fabric. Going from the right to the left side in the target area, such layered areas are the following (Fig. 7A): (1) a ferric and sulfate-rich layer depleted in silica, (2) an iron- and sulfate-rich intermixing intermediate layer intermixing with silica, and (3) a silica-rich layer with sulfate compounds and low ferric concentration. The co-occurrence of iron and sulfate anions is consistent with a mineral matrix formed by the precipitation of ferric oxysulfates. They precipitate out from acidic solutions (pH <3) through the microbial attack on the subsurface orebody, which releases high amounts of SO_4^-, Fe^{3+}, and H^+ (Gómez-Ortiz *et al.,* 2014; Fernández-Remolar *et al.,* 2018). As acidic conditions usually inhibit silica precipitation, its presence as a component of some underground laminations likely occurred under different geochemical constraints.

The alternation between ferric- and sulfate-rich and silica-bearing layers suggests seasonal or temporal chemical

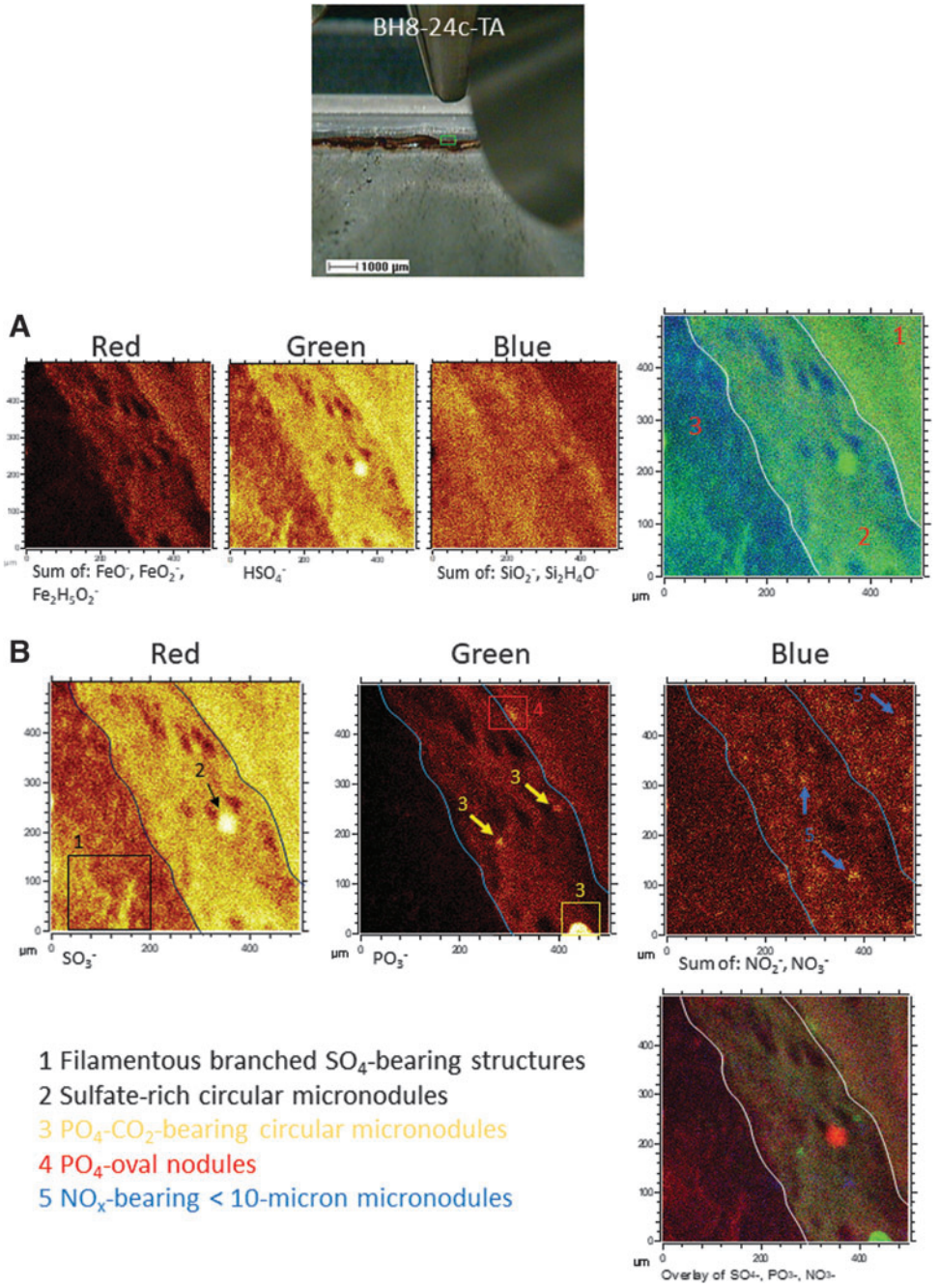

FIG. 7. (**A**) Red, green, and blue image combination for Fe-, S-, and Si-bearing inorganic anions which show compositional changes in laminations including a ferric and sulfate-rich lamina (1), an intermediate ferric and sulfate lamina with silica (2), and a silica-rich layer with secondary sulfate (3). (**B**) Red, green, and blue image combination for SO_3^-, PO_3^-, and NO_2^- + NO_3^- inorganic anions which allow recognizing different microstructures of biological origin as (1) filamentous branched SO_4-bearing structures, (2) sulfate-rich circular micronodules, (3) PO_4^- and CO_2^--bearing circular micronodules, (4) PO_4-bearing oval nodules, and (5) NO_x-bearing <10-micron size micronodules. The ToF-SIMS ion images were collected and processed from the target area TA.

variations in pH and/or redox. The microbial activity has been claimed to trigger microenvironmental changes such as alkalinization, leading to silica precipitation in a sulfate-rich deposit (Birnbaum and Wireman, 1984, 1985). Neutralization of acidic solutions has been reported in Río Tinto through microbial reduction of the ferric ion and precipitation of carbonate (Fernández-Remolar *et al.,* 2012). However, whether the microbial activity was involved in the silica precipitation is unclear since an increase in the pH through diagenesis could have also triggered the silica precipitation. In the Río Tinto acidic materials, neutralization has been associated with ferric oxysulfate exhumation and exposition to rainwater (Fernández-Remolar and Knoll, 2008). The percolating meteoric solutions would have increased the pH

of the ferric deposits, washed down, and co-precipitated sulfates and silica. Consequently, the alternation between laminae of ferric oxysulfates and silica-rich layers (Fig. 7A) could have recorded in a few millimeters a full cycle of the Río Tinto gossan formation, including both acidic alteration and maturation stages.

In this mineral substrate, the ToF-SIMS mapping analysis has identified several microstructures bearing essential anions for life (Figs. 4C and 7B). They correspond to the following five elements recording potential metabolic information (Fig. 7B): (1) 40-micron size circular nodules enriched in sulfate ions; (2) >100-micron long sulfate-rich filamentous structures with straight to sinuous branched trajectory; (3) >40 micron-sized circular nodule mineralized by inorganic PO_4-bearing compounds; (4) <20-micron sized oval nodule with PO_4-bearing lipid traces; and (5) <15 micron-sized nodules with NO_2^- and NO_3^- anions. The occurrence of different microstructures that are identified by their anion composition suggests that they have been formed by other abiotic and/or microbial processes.

The abundance of sulfate in the subsurface (Fernández-Remolar *et al.,* 2008) suggests that the mineralization of different structures by this anion has been the result of a protonation reaction on the microbial surface as a consequence of a low pH (Konhauser and Riding, 2012). The formation of a predominantly protonated microbial surface has likely favored a preferential binding of the available negative ions in the Río Tinto subsurface as SO_4^- leading to the mineralization of the biological structures. The detection of different organic compounds bearing SO_x ($x = 2–7$) groups strongly supports that the sulfate mineralization proceeded through a direct binding between the protonated biomolecular surface and sulfate anion that was highly available in the subsurface solutions. Acidic fungi and tolerant plants have been reported as active agents of biomineralization of jarosite ($KFe^{3+}{}_3(OH)_6(SO_4)_2$) (Rodríguez *et al.,* 2005; Oggerin *et al.,* 2013), and the biological activity plays an essential role in the fluvial basin sedimentation by sulfate biomineralization in biofilms (Fernández-Remolar *et al.,* 2010), where it has also been recognized in ancient Río Tinto sediments (Fernández-Remolar *et al.,* 2005). The ToF-SIMS image analysis of terrace and gossan samples currently shows the presence of sulfate and cholesteryl sulfate associated with larger biological structures (Fig. 8). The occurrence of cholesteryl derivatives strongly supports that they correspond to different eukaryotic forms that inhabited the acidic basin more than 6 million years ago (Fernández-Remolar and Knoll, 2008). In this regard, the SO_4-bearing branched filamentous structure (Figs. 2E, 4C2, and 7B) could represent a large prokaryotic filament as it is also composed of likely N-bearing fragments like amino acids (Fig. 4A1). The circular structure has, in turn, an unknown

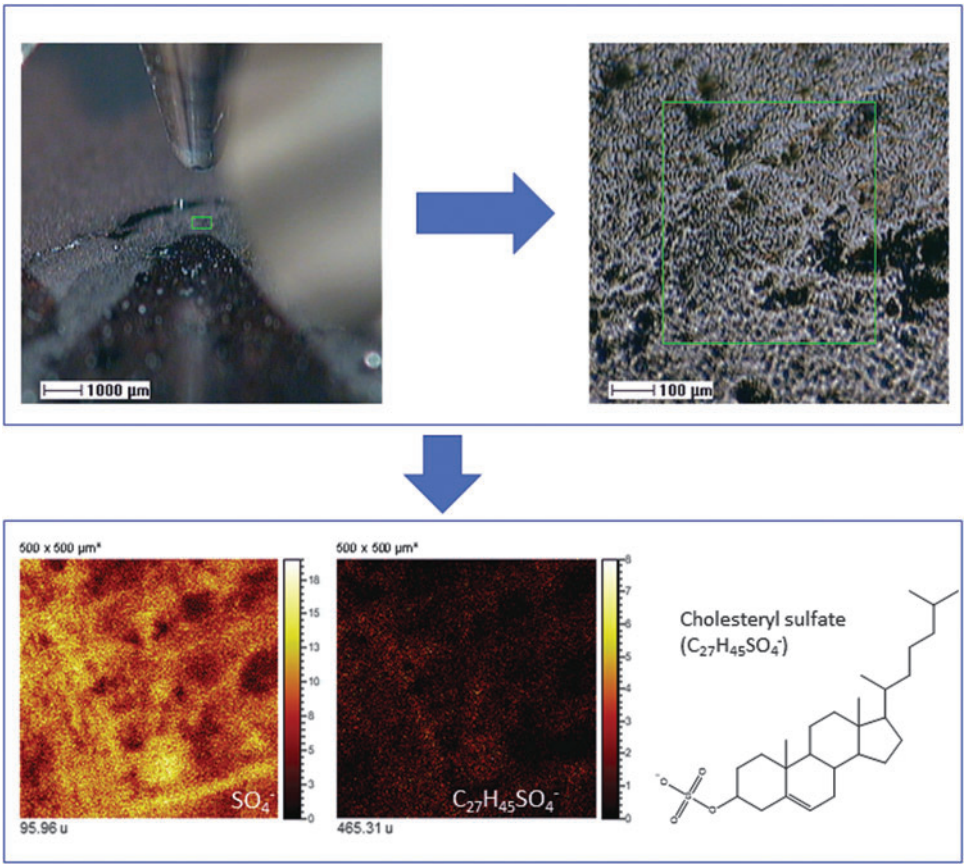

FIG. 8. The occurrence of SO_4^- and $C_{27}H_{45}SO_4^-$ (cholesteryl sulfate $[M - H]^-$ ion) in samples from the Upper Gossan in Pena de Hierro (~25 Ma) mapping different remains of eukaryotic structures containing cholesterol. Cholesteryl sulfate has not been found in the BH8-24c sample occurring in the subsurface, supporting a negligible content in steroids, which is consistent with a sample preserving compounds produced by subsurface prokaryotes.

origin and could have been formed either through abiotic or biotic mineralization. In both cases, the sulfate mineralization does not depend on the metabolic process itself but on the high availability of sulfate that promoted the mineralization of biological and nonbiological structures in the Río Tinto subsurface.

As discussed above, the second group of microstructures has been outlined by the occurrence of PO_2^- and PO_3^- anions. They correspond to two different morphologies that include both circular and ovoidal shapes, which are associated with different compounds. The circular morphology meets the distribution of anion CHO_2^- which could be a major fragment of carbonates. In turn, the PO_4-bearing ovoidal structure is associated with a set of several compounds that have been tentatively assigned to different lipid anions like phospholipids (Mazzella *et al.,* 2005; Heim *et al.,* 2009). Such a compositional difference suggests that while the circular microstructures preserve a biomineralized microstructure by carbonate and phosphate (Fernández-Remolar *et al.,* 2012, 2018; Sánchez-Román *et al.,* 2014, 2015), the smaller and ovoidal elements could correspond to the preservation of a microbial population that has been mineralized by oxysulfates. An alternative explanation for the different molecular composition in the phosphatic micronodules could also be related to the number of preserved cells. In this regard, fewer biomineralized cells will lower the concentration in lipids that would accordingly decrease the intensity below the intensity levels to be plotted as a ToF-SIMS molecular image. Although this could be a plausible explanation, we observed that the largest phosphatic nodule, which

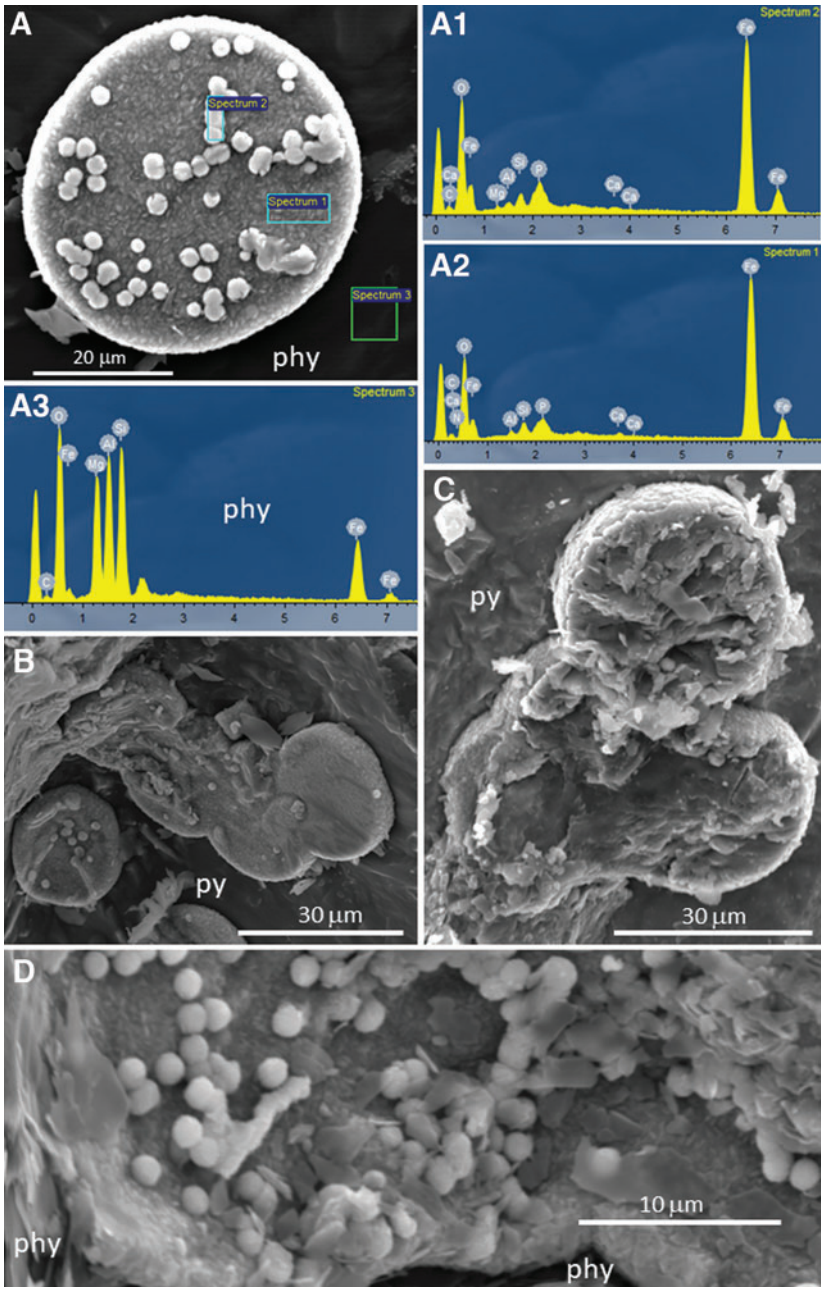

FIG. 9. Image and compositional analysis by SEM-EDS of sample BH4-60a, collected at 151.5 m deep in borehole BH4 (Fernández-Remolar *et al.,* 2008). It shows the occurrence of discoidal (**A** and **B**) to spheroidal (**C**) nodules that grew on a siliceous-rich (phy) and pyritic (py) substrate, respectively. The elemental analysis of the nodular microstructures is composed mainly of C, Fe, and P (see EDS spec in A1 and A2), while in the case of the discoidal structure, the mineral substrate is a phyllosilicate (A3). It evidences that the morphology is strongly dependent on the substrate as it provides the electron donor for the metabolic process involved in the structure formation. The high C and Fe content has been interpreted as a siderite-rich composition ($FeCO_3$) accompanied by organic compounds and with a secondary phosphate mineral. The nodule microstructure is also accompanied with spheric elements (see A, B, and **D**) that could be siderite nanoglobules or microspherules, which have been reported in precipitates of Río Tinto microbial cultures (Sánchez-Román *et al.,* 2014).

should have biomineralized a more significant number of cells, does not show any evidence of lipids, suggesting that such an explanation does not elucidate the compositional changes in the different phosphatic nodules. Consequently, it is more likely that differential composition in the PO_3-bearing micronodules results from the metabolic activity by chemoheterotrophs that produced biomineralized structures which composition was mainly mineral.

Indeed, similar spheroidal microstructures composed of carbonate and phosphate (Fig. 9) have been reported in surface and subsurface areas of Río Tinto (Fernández-Remolar *et al.,* 2012, 2018). The SEM-EDS analysis of samples collected in borehole BH4 (Fernández-Remolar *et al.,* 2008) shows that they consist of >30–60 micronodular elements with discoidal to spherical morphology whose primary mineral composition varies from ankerite ($CaFe^{2+}(CO_3)_2$) to siderite ($FeCO_3$), and likely different amounts of phosphate. The carbonate and phosphate biomineralization could have been associated with chemoheterotrophic metabolism (*e.g., Acidiphilium* sp.), which would have oxidized organic matter by using ferric ion as an electron acceptor (Sánchez-Román *et al.,* 2014; Fernández-Remolar *et al.,* 2018). Recent experiments have shown that *Tessaracoccus lapidicaptus,* a heterotrophic bacteria isolated from the Río Tinto basement at 297 m deep (Sánchez-Román *et al.,* 2015), precipitates siderite and vivianite ($Fe_3(PO_4)_2 \cdot 8H_2O$) in cell walls and the EPS. Interestingly, *T. lapidicaptus* reduces NO_3^- as it uses this anion as an electron acceptor, which means that it could recycle nitrogen in the subsurface of the IPB.

The ToF-SIMS mapping ability has also provided information to identify tiny micronodules (<15 microns), which are enriched in NO_2^- and NO_3^- (Fig. 7B). The microstructure proportions (<10 microns) fit well with the thickness of microfilament sections (Fig. 2C, 2D), which also have a high content in elemental N ($\sim$9 atomic % $\approx$ 9 weight %). In addition, the microfilaments also show a primary elemental composition dominated by C, O, and Fe, suggesting a siderite-like mineral composition. The co-occurrence of elemental Si as a secondary composition supports a pH increment during the formation of carbonates in the filament interior. The SEM images show that the microfilaments are currently entrenching the lamination surface, suggesting that they likely grew through the mineral surface dissolution (Fig. 2C). Assuming that the outermost part of a layer is composed of iron oxyhydroxides and oxysulfates (Fig. 2C, 2D), the attack process could be related to the reduction of Fe^{3+} and/or SO_4^-. The electron donors could have been different compounds like organic molecules such as CH_4 (Puente-Sánchez *et al.,* 2014), leading to the nucleation of siderite (Drake *et al.,* 2017; Fernández-Remolar *et al.,* 2018; Leandro *et al.,* 2018) but also the formation of nitrate as a final member of the ammonia oxidation that uses the ferric cation as an electron acceptor as the Feammox bacteria (in 't Zandt *et al.,* 2018). Feammox bacteria use the ferric cation as an electron acceptor through ammonia oxidation where dinitrogen gas, nitrite, or nitrate are released as a final by-product. In the microbial attack on the ferric surface, SO_4^- ions could also be available as the electron acceptor for different metabolic pathways, including autotrophic and heterochemotrophic (Zhang *et al.,* 2009; Drake *et al.,* 2017). Furthermore, the oxidized nitrogen compounds could also be recycled by using ammonia as an electron donor (in 't Zandt *et al.,* 2018). Under such metabolic activity, NO_2^- and NO_3^- are by-products that would accumulate inside the microfilament structure as it is evidenced by ToF-SIMS and SEM-EDS results (Figs. 2C–2E, 4C4, 7B, and 10).

The ToF-SIMS mapping in another target area of sample BH8-24c provides further information about the source of nitrogen in the subsurface. The imaging analysis of the positive ions at 18.04, corresponding to NH_4^+, provides a full-frame of the nitrogen cycle if the NO_2^- and NO_3^- mapping is included in the analysis (Fig. 11). It shows the occurrence of the different nitrogen molecular species following an inverse distribution where the NH_4^+ and NO_3^- ions occur in opposite areas, while the NO_2^- co-occurs with areas with both ammonium and nitrate species. Such distribution suggests that NO_2^- is an intermediate specie that could be formed through the microbial oxidation of NH_4^+ microlocations and recycled by microbial reduction of NO_3^-. The ammonia distribution meets the occurrence of some amino acid fragments (*e.g.,* $C_2H_8N^+$ in Fig. 11), suggesting that the NH_4^+ production results from the ammonification of

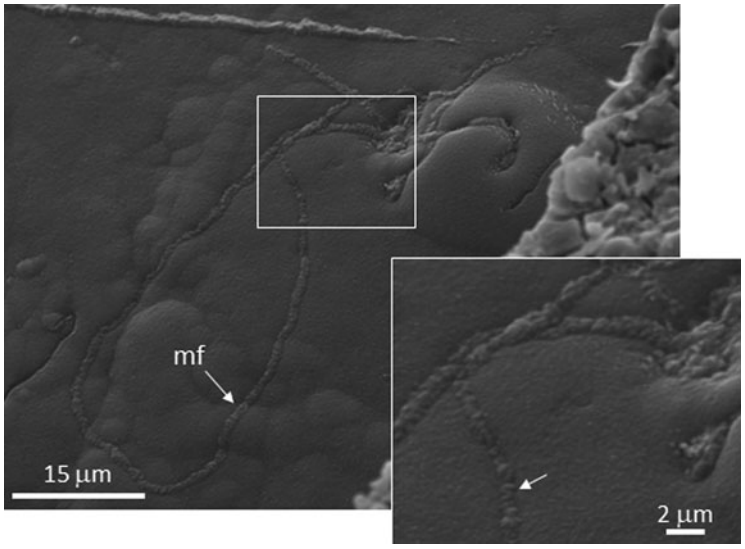

FIG. 10. SEM image of the BH8-24c sample collected at $\sim$40 m deep. It shows the microfilament (mf) morphology and microstructure interior, which seems filled by different minor elements (<0.5 microns) with filamentous or rod-like shape.

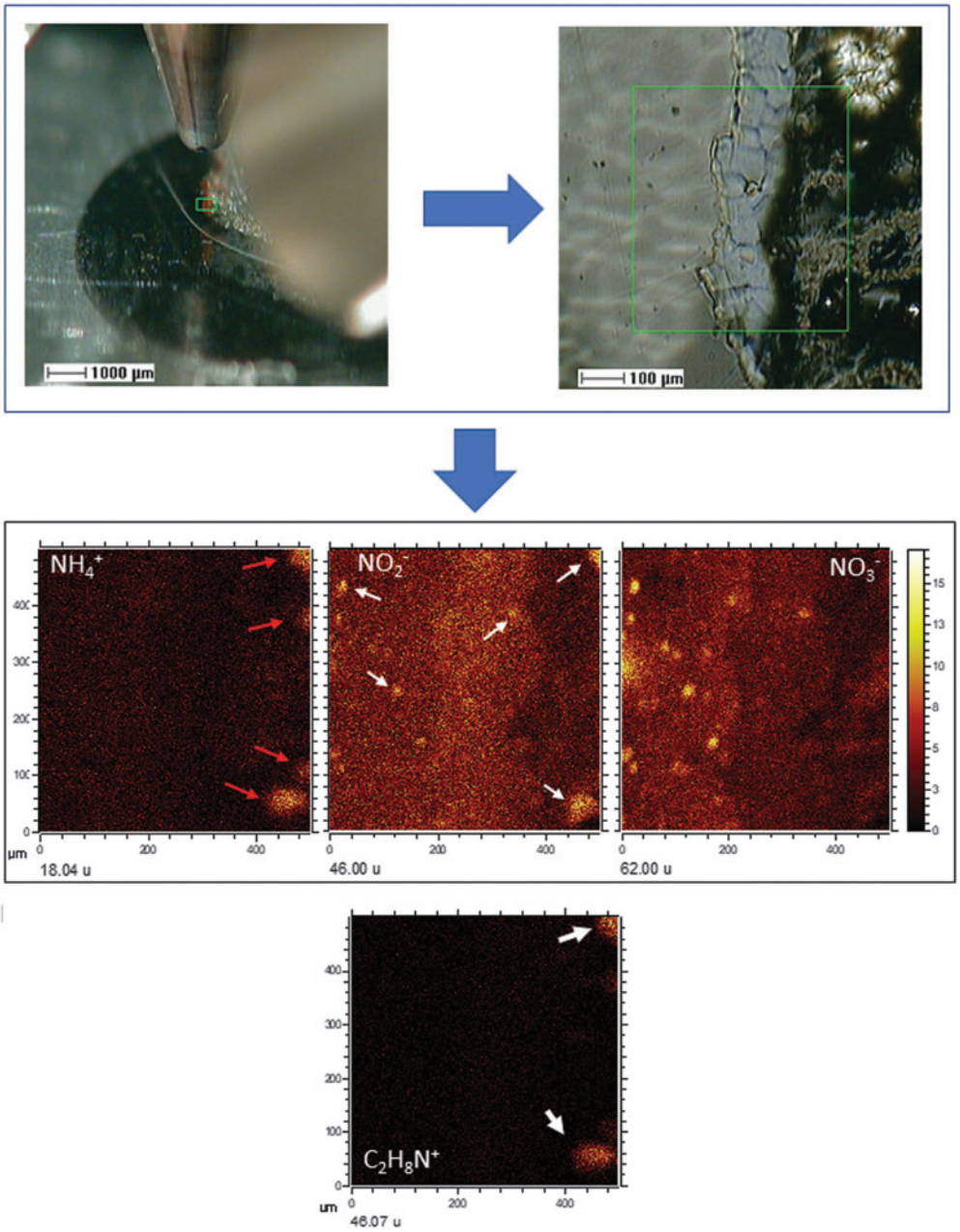

FIG. 11. ToF-SIMS image of another target area in sample BH8-24c showing the distribution of positive and negative N-bearing ions as NH_4^+, NO_2^-, and NO_3^- which provide some insight of how the nitrogen cycle could operate in the subsurface. This could be partly initiated by ammonification (red arrows) in areas enriched with peptidic chains, which would be released to other microlocations where the NH_4^+ will be oxidized to nitrite and nitrate by microbes that formed the microfilaments. The comparison between the three intensity distribution images shows that NO_2^- (white arrows) appears as an intermediate compound that co-occurs in the NH_4^+- and NO_3^--rich micronodules.

biological compounds like proteins (Herbert, 1999). While the ammonium can be recycled by ammonification of biological nitrogen, the primary source of nitrogen is a questionable matter. Although it could be expected the occurrence of organic compounds fitting the distribution of NO_2^- and NO_3^-, we have found no evidence of large molecular compounds associated with such distribution. While this could be a consequence of the mass spectral range limited up to 750 Da, the small size of the microstructures containing the N-bearing anions should also have a low concentration in lipids, as can be estimated from the SEM images. The ToF-SIMS images show that the NO_2^- and NO_3^- microstructures have size smaller than 10 microns (Fig. 11), which correspond to <50 cell bodies as recognized in the SEM images (Fig. 9). As the lipidic content should be low as the cellular remains have experienced mineralization and degradation, it is expected that the molecular concentration be low enough to have a clear signal above the spectral data background.

Rock leachates of samples BH8 collected at 40 m deep corresponding to the weathered hydrothermal stockwork (Fernández-Remolar *et al.,* 2008) have shown that it can

release up to 0.2–2 ppm of NO_3^-, while the NO_2^- concentration was around 72 ppm. Rock samples of nonweathered stockwork materials (Fernández-Remolar *et al.,* 2008) sampled below 140 m deep released up to 50 ppm NO_2^- but, in turn, a NO_3^- concentration lower than 0.02 ppm. We suggest that the primary source of nitrogen could be the nitrite ion produced during the Carboniferous hydrothermal activity (Leistel *et al.,* 1998; Almodóvar and Sáez, 2004). Hydrothermal systems have been reported to be associated with the transfer and formation of nitrates by the volatilization of ammonia and dinitrogen gas from Earth's crust, as well as through nitrite and nitrate leaching of underlying sedimentary, igneous, and metamorphic rocks by hydrothermal fluids (Holloway and Dahlgren, 2002). The chemical analysis of subsurface fluids from multilevel diffusion samplers in BH8 (Fernández-Remolar *et al.,* 2008) shows a NO_3^- concentration lower than 4.2 ppm ($\sim$67 μM), suggesting that it is a transitional reservoir that receives nitrogen from meteoric replenishment and the basement alteration. Such a weathering process could be accelerated during ancient thermal episodes that led to the formation of the Gossan and oldest terraces of Río Tinto during different thermal episodes (Fernández-Remolar *et al.,* 2005; Essalhi *et al.,* 2011; Velasco *et al.,* 2013).

The ToF-SIMS surface analysis has also shown that other anions like Cl^- follow the distribution pattern of NO_2^- and NO_3^- (Fig. 4C1), which occur inside the microfilament structures (Figs. 2C, 2D, and 4C4). Leachates of samples recovered at 40 m depth, where the weathered stockwork is found, gave a Cl^- concentration of around 8.5 ppm. However, chloride was increased up to 72.5 ppm in pristine hydrothermal materials occurring below 140 m depth. The analysis of underground water samples from the multilevel diffusion samplers (Fernández-Remolar *et al.,* 2008) in BH8 provided a chloride concentration of up to 290 ppm (8200 μM). Although the Cl^- distribution in the subsurface suggests that it is released from the hydrothermal materials like the nitrogen anions, it experiences an increment in the subsurface fluids. This could have resulted from an additional supply from other sources (*e.g.,* rainwater) or that it was not taken up by microbial activity at the same rate as nitrate.

The distribution of the main biomolecular groups that have been listed above provides additional information about the microbial communities occurring in the Río Tinto subsurface. In this regard, the N-bearing compounds associated with the preservation of amino acid, as well as the occurrence pattern of saccharides, are homogeneously distributed in the target area analyzed by ToF-SIMS. However, some slight variations depend on the anion type. The CN^-, CON^-, and the N-bearing anions interpreted as amino acid fragments, and likely N-bearing lipids, show a higher affinity to the distribution of silica anions (Fig. 4A). In turn, the occurrence of CP^- and CNP^- anions is more akin to the distribution pattern of the Fe- and S-bearing inorganic anions, as the P-bearing lipid fragments do (Fig. 6B). Both N- and P-bearing major anions, as well as the HS^- anion, have a higher affinity for the filamentous structure enriched in sulfate that is present in the lower-left corner of the sample (Figs. 4A, 4C, and 7B). Such a complementary distribution suggests a change in the microbial community that would follow the increment of silica in the laminations (Fig. 7A) or alternation in the preservation conditions resulting from environmental and/or diagenesis changes. In the first case, such a variation will go from communities that would produce a higher content in P-bearing lipids during a ferric-rich episode (Figs. 6B and 7B) to an increment in prokaryotic forms synthesizing N-bearing biomolecules during the episode precipitating silica (Figs. 4A and 7A), which could be associated with an increment in the EPS formation by microbial communities (Escudero *et al.,* 2018). Interestingly, the saturated and monounsaturated FAs follow the general pattern shown by lipids greater than 600 Da. This could be related to the environmental alternation from ferric-rich and acidic solutions to more neutral, where the silica formation was favored. It could come together with a change in the preservation or environmental conditions affecting the microbial composition.

The ToF-SIMS analytic capabilities have also mapped the distribution of different *m/z* fragments that are characteristic of other saccharides. Although the distribution is more homogeneous, it follows the main laminae fabric and shows a slight intensity increment in the iron-rich laminae (Figs. 4C and 6D). The occurrence of a regular distribution of saccharides in the target area suggests multiple origins. As discussed above, saccharides occur in head groups of membrane lipids, such as sphingolipids or saccharolipids, but are also found as polysaccharides in EPS. However, in terms of quantity, EPS produce larger amounts of biological compounds compared to membrane lipids and would be the primary source of saccharides in the subsurface. This is consistent with novel findings suggesting that biofilm growth in the subsurface is a common microbial process in the Río Tinto subsurface (Escudero *et al.,* 2018).

6. Conclusions

The combination of the composition and distribution of different molecules assigned to an inorganic or organic origin provides a piece of evidence to distinguish microbial structures that have resulted from the metabolic cycling of elements in the Río Tinto subsurface. Based on such information, at least four groups of microstructures of microbial origin can be recognized as the following:

(A) **Branched macrofilaments**. Mineralized structures with sulfate and enriched in N-bearing biomolecular fragments like amino acids and/or lipids. The release of organic compounds bound to sulfate groups suggests that the structure surface could be protonated or saturated with different cations. Although the metabolism of the microorganism that produced such structures is unknown, it may unlikely be related to iron or sulfur bacteria, as they are not affecting the mineral surfaces of ferric oxysulfate laminations (Figs. 2C, 4A, and 7B).

(B) **Ovoidal nodules with PO_4-lipids**. Size and composition suggest that they could result from the mineralization of bacterial colonies by ferric oxysulfates. As the nodule size usually is smaller than 30 microns in length (Fig. 6B), the structure could have resulted from biofilms of bacteria that were mineralized by ferruginous oxysulfates under acidic conditions.

(C) **Mineralized nodules of heterochemotrophic bacteria**. They were likely produced through the metabolic activity of Actinobacteria and/or Alphaproteobacteria as *Tessaracoccus* and/or *Acidiphilium* by the precipitation of

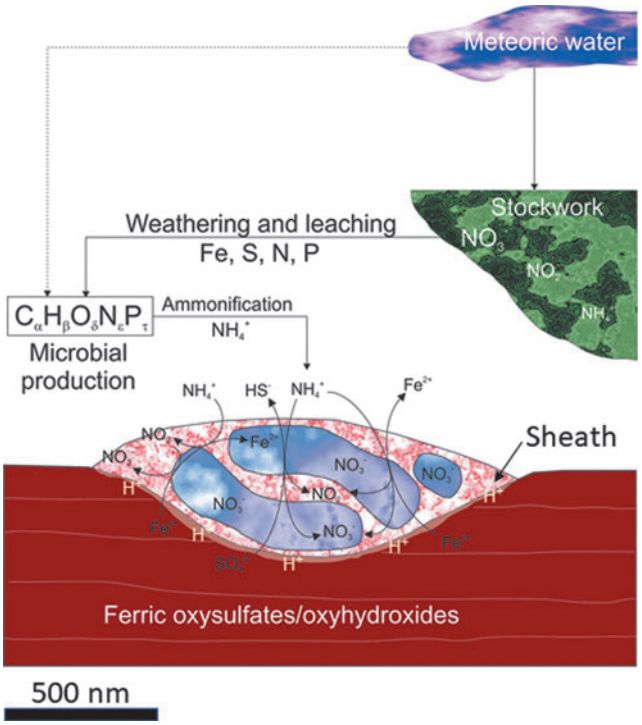

FIG. 12. Image showing an idealized section of the microfilaments describing the biogeochemical pathways of NO_2^- and NO_3^-. The ammonia distribution in the sample suggests that it comes from the microbial ammonification of peptide-based compounds which could be eventually used as an electron donor to reduce the ferric iron found in the oxysulfates and/or oxyhydroxides. The ammonia would be oxidized to produce nitrite and nitrates. The microbial attack would release the ferric ion through using different organic acids (*e.g.,* oxalic) and/or siderophores, which would dissolve the lamination surface. Although ammonification could be the transitional source of nitrogen, the high content of nitrogen in the stockwork suggests that it can be the primary source of nitrogen. However, the meteoric water could also act as a minor source as well. The occurrence of elemental C in the microfilaments brings up carbonate as the main mineralizing component with some remaining organic compounds.

carbonate and phosphate around the cellular structure and inside the EPS matrix. Such microorganisms would use the ferric oxysulfate surface dissolution that would release the ferric ion, which would be used as the electron acceptor through the oxidation of organic compounds (Fernández-Remolar *et al.,* 2012; Sánchez-Román *et al.,* 2014, 2015). The carbonate and phosphate mineralization centers merged to form spheroidal or discoidal structures (Fig. 9). Such a mineralization process was likely favored by a fast pH increment at a cellular scale by producing bicarbonate anions from the metabolic oxidation of organic matter (Sánchez-Román *et al.,* 2014). The siderite precipitation through the pyrite dissolution must be associated with the production of ferric and/or sulfate ions, which can be used by aerobic or anaerobic chemoheterotrophic microbes that use them as electron acceptors like *Acidithiobacillus* spp. and *Leptospirillum* sp. (Sand *et al.,* 2001; Amils *et al.,* 2013) or by denitrifying bacteria (Hayakawa *et al.,* 2013). In this case, the process should be carried out by living forms that can change the metabolic activity depending on nutrient availability or the development of microbial consortia having both chemoheterotrophic and chemosynthetic bacteria.

(D) **Microfilaments of nitrogen bacteria**. They were formed by microbes that metabolized ammonium and nitrite to produce nitrate as an endmember (Figs. 2C–2E, 4C4, and 7B). Intriguingly, the structures that contain the oxidized nitrate anions seem sheathed colonies of smaller microbial bodies that grew following the microfilament direction along the surface lamina (Fig. 9). The process could have occurred through the microbial attack on the oxysulfate/oxyhydroxide surface (Fig. 12), which would release ferric ions as has been described in some bacteria (Bonneville *et al.,* 2004; Kraemer 2004). Thus, it would be available as an electron acceptor through ammonia and nitrite oxidation (in 't Zandt *et al.,* 2018).

Here, we provided mineralogical and biomolecular evidence that different mineralized structures in the Río Tinto basement were formed by the interaction of the microbial communities with the geological substrate. Its proposed formation demonstrates how the biosphere has developed through the preexistent chemical cycles that have been maintained by the geological activity over billions of years. In the Río Tinto case, the microbial communities have produced some structures that can be unequivocally identified as byproducts of the existence of biochemical cycles that have been powered by the underground metabolic activity of chemoheterotrophic and chemosynthetic life. Such biogeochemical cycling was accompanied by mineralization driven by the production of sulfate and ferric iron sourced in the biooxidation of the sulfide orebody by chemolithotrophic life. Such a process was intimately integrated into the transfer of matter and energy in the Río Tinto subsurface habitats and became the principal agent to preserve the biological information of the underground microbial communities.

Acknowledgments

The authors are grateful for the ideas provided by several reviewers who have contributed greatly to improve the manuscript. David Fernández-Remolar acknowledges the full support provided by the Director of the SKL Lunar and Planetary Sciences Keke Zhang.

Author Contribution

DCFR, DGO, and TH wrote the manuscript with input from RA, NR, NB, AA, and CE. DCFR, TH, and NB ran the ToF-SIMS analysis. DCFR and NR collected the SEM-EDS data. RA, NR, and CE provided microbial information for data interpretation. All authors contributed to the discussion and final manuscript.

Funding

This research has been supported by the Fundo de Desenvolvimento das Cientifico e da Tecnologia da RAE de Macau (proposals FDCT-0005-2020-A1 and FDCT-18-024-SSI), and the project on Civil Aerospace Technologies No. D020303 funded by China National Space Administration. Samples of borehole BH8 were collected during the ground

drilling operations funded by the NRA-02-OSS-01 NASA-ASTEP ''Mars Astrobiology Research and Technology Experiment (MARTE),'' a Mars analog drilling project to search for subsurface life at RÚo Tinto. Y.S. acknowledges funding by FDCT (No. 0002/2019/APD). N.B. acknowledges funding from NSERC.

Author Disclosure Statement

The authors declare that the research was conducted in the absence of any commercial or financial relationships that could be construed as a potential conflict of interest.

Supplementary Material

Supplementary Table S1
Supplementary Table S2
Supplementary Figure S1

References

Almodóvar GR and Sáez R (2004) Los sulfuros masivos de la Faja Pirítica Ibérica. In *Geología de España,* edited by JA Veras. Sociedad Geológica de España: Instituto Geológico y Minero de España, Madrid, pp 207–209.

Amils R, Fernández-Remolar DC, Parro V, *et al.* (2013) Iberian Pyrite Belt Subsurface Life (IPBSL), a drilling project of biohydrometallurgical interest. *Adv Mat Res* 825:15–18.

Birnbaum SJ and Wireman JW (1984) Bacterial sulfate reduction and pH: implications for early diagenesis. *Chem Geol* 43: 143–149.

Birnbaum SJ and Wireman JW (1985) Sulfate-reducing bacteria and silica solubility: a possible mechanism for evaporite diagenesis and silica precipitation in banded iron formations. *Can J Earth Sci* 22:1904–1909.

Bonneville S, Van Cappellen P, and Behrends T (2004) Microbial reduction of iron(III) oxyhydroxides: effects of mineral solubility and availability. *Chem Geol* 212:255–268.

Brantley SL, Lebedeva M, and Hausrath EM (2012) A geobiological view of weathering and erosion. In *Fundamentals of Geobiology,* edited by AH Knoll, D Canfield, and K Konhausers. Wiley, Oxford, UK, pp 205–227.

Bühring SI, Schubotz F, Harms C, *et al.* (2012) Lipid signatures of acidophilic microbial communities in an extreme acidic environment—Río Tinto, Spain. *Org Geochem* 47:66–77.

Cady SL, Farmer JD, Grotzinger JP, *et al.* (2003) Morphological biosignatures and the search for life on Mars. *Astrobiology* 3:351–368.

Colín-García M, Kanawati B, Harir M, *et al.* (2011) Detection of peptidic sequences in the ancient acidic sediments of Río Tinto, Spain. *Orig Life Evol Biosph* 41:523–527.

Del Poeta M, Nimrichter L, Rodrigues ML, *et al.* (2014) Synthesis and biological properties of fungal glucosylceramide. *PLoS Pathogens* 10, doi:10.1371/journal.ppat.1003832.

Drake H, Ivarsson M, Bengtson S, *et al.* (2017) Anaerobic consortia of fungi and sulfate reducing bacteria in deep granite fractures. *Nat Commun* 8, doi:10.1038/s41467-017-00094-6.

Escudero C, Vera M, Oggerin M, *et al.* (2018) Active microbial biofilms in deep poor porous continental subsurface rocks. *Sci Rep* 8, doi:10.1038/s41598-018-19903-z.

Essalhi M, Sizaret S, Barbanson L, *et al.* (2011) A case study of the internal structures of gossans and weathering processes in the Iberian Pyrite Belt using magnetic fabrics and paleomagnetic dating. *Miner Depos* 46:981–999.

Fahy E, Subramaniam S, Brown HA, *et al.* (2005) A comprehensive classification system for lipids. *J Lipid Res* 46:839–862.

Fernández-Remolar DC and Knoll AH (2008) Fossilization potential of iron-bearing minerals in acidic environments of Rio Tinto, Spain: implications for Mars exploration. *Icarus* 194:72–85.

Fernández-Remolar DC, Morris RV, Gruener JE, *et al.* (2005) The Rio Tinto Basin, Spain: mineralogy, sedimentary geobiology, and implications for interpretation of outcrop rocks at Meridiani Planum, Mars. *Earth Planet Sci Lett* 240:149–167.

Fernández-Remolar DC, Prieto-Ballesteros O, Rodríguez N, *et al.* (2008) Underground habitats in the Río Tinto Basin: a model for subsurface life habitats on Mars. *Astrobiology* 8: 1023–1047.

Fernández-Remolar DC, Gómez-Ortíz D, Prieto-Ballesteros O, *et al.* (2010) Fluvial bedform generation by biofilm activity in the Berrocal Segment of Río Tinto: acidic biofilms and sedimentation. In *Microbial Mats: Modern and Ancient Microorganisms in Stratified Systems,* edited by J Seckbach and A Orens. Springer, Dordrecht, the Netherlands, pp 483–498.

Fernández-Remolar DC, Prieto-Ballesteros O, Gómez-Ortíz D, *et al.* (2011) Río Tinto sedimentary mineral assemblages: a terrestrial perspective that suggests some formation pathways of phyllosilicates on Mars. *Icarus* 211:114–138.

Fernández-Remolar DC, Preston LJ, Sánchez-Román M, *et al.* (2012) Carbonate precipitation under bulk acidic conditions as a potential biosignature for searching life on Mars. *Earth Planet Sci Lett* 351:13–26.

Fernández-Remolar DC, Santamaría J, Amils R, *et al.* (2015) Formation of iron-rich shelled structures by microbial communities. *J Geophys Res Biogeosciences* 120:147–168.

Fernández-Remolar DC, Banerjee N, Gómez-Ortiz D, *et al.* (2018) A mineralogical archive of the biogeochemical sulfur cycle preserved in the subsurface of the Río Tinto system. *Am Mineral* 103:394–411.

Gómez-Ortiz D, Fernández-Remolar DC, Granda Á, *et al.* (2014) Identification of the subsurface sulfide bodies responsible for acidity in Río Tinto source water, Spain. *Earth Planet Sci Lett* 391:36–41.

Harwood JL and Russell NJ (1984) *Lipids in Plants and Microbes.* George Allen & Unwin, London.

Hayakawa A, Hatakeyama M, Asano R, *et al.* (2013) Nitrate reduction coupled with pyrite oxidation in the surface sediments of a sulfide-rich ecosystem. *J Geophys Res Biogeosciences* 118:639–649.

Hazen RM (2012) Geochemical origins of life. In *Fundamentals of Geobiology,* edited by AH Knoll, D Canfield and K Konhausers. Wiley, Oxford, UK, pp 315–332.

Hazen RM, Papineau D, Bleeker W, *et al.* (2008) Mineral evolution. *Am Mineral* 93:1693–1720.

Heim C, Sjövall P, Lausmaa J, *et al.* (2009) Spectral characterisation of eight glycerolipids and their detection in natural samples using time-of-flight secondary ion mass spectrometry. *Rapid Commun Mass Spectrom* 23:2741–2753.

Herbert RA (1999) Nitrogen cycling in coastal marine ecosystems. *FEMS Microbiol Rev* 23:563–590.

Holloway JM and Dahlgren RA (2002) Nitrogen in rock: occurrences and biogeochemical implications. *Global Biogeochem Cycles* 16:65-1–65-17.

in 't Zandt MH, de Jong AEE, Slomp CP, *et al.* (2018) The hunt for the most-wanted chemolithoautotrophic spookmicrobes. *FEMS Microbiol Ecol* 94, doi:10.1093/femsec/fiy064.

Kawecki M and Bernard L (2018) Database of proteinogenic amino acid reference spectra for bismuth-cluster ToF-SIMS. I. Negative polarity. *Surface Science Spectra* 25, doi:10.1116/1.5024987.

Killops SD and Killops V (2005) *Introduction to Organic Chemistry.* Blackwell Science, Oxford, UK.

Konhauser K and Riding R (2012) Bacterial biomineralization. In *Fundamentals of Geobiology.* Blackwell Publishing, Oxford, UK, pp 105–130.

Kraemer SM (2004) Iron oxide dissolution and solubility in the presence of siderophores. *Aquat Sci* 66:3–18.

Leandro T, Rodriguez N, Rojas P, *et al.* (2018) Study of methanogenic enrichment cultures of rock cores from the deep subsurface of the Iberian Pyritic Belt. *Heliyon* 4, doi:10.1016/j.heliyon.2018.e00605.

Leistel JM, Marcoux E, Thiéblemont D, *et al.* (1998) The volcanic-hosted massive sulphide deposits of the Iberian Pyrite Belt. *Mineralium Deposita* 33:2–30.

Lyons TW, Reinhard CT, and Planavsky NJ (2014) The rise of oxygen in Earth's early ocean and atmosphere. *Nature* 506: 307–315.

Mazzella N, Molinet J, Syakti AD, *et al.* (2005) Use of electrospray ionization mass spectrometry for profiling of crude oil effects on the phospholipid molecular species of two marine bacteria. *Rapid Commun Mass Spectrom* 19:3579–3588.

Nealson KH and Rye R (2014) Evolution of metabolism. In *Treatise on Geochemistry (Second Edition),* edited by HD Holland and KK Turekians. Elsevier, Oxford, UK, pp 43–59.

Oggerin M, Tornos F, Rodríguez N, *et al.* (2013) Specific jarosite biomineralization by *Purpureocillium lilacinum,* an acidophilic fungi isolated from Río Tinto. *Environ Microbiol* 15:2228–2237.

Olsen I and Jantzen E (2001) Sphingolipids in bacteria and fungi. *Anaerobe* 7:103–112.

Puente-Sánchez F, Moreno-Paz M, Rivas LA, *et al.* (2014) Deep subsurface sulfate reduction and methanogenesis in the Iberian Pyrite Belt revealed through geochemistry and molecular biomarkers. *Geobiology* 12:34–47.

Rodríguez N, Menéndez N, Tornero J, *et al.* (2005) Internal iron biomineralization in *Imperata cylindrica,* a perennial grass: chemical composition, speciation and plant localization. *New Phytol* 165:781–789.

Sánchez-Román M, Fernández-Remolar D, Amils R, *et al.* (2014) Microbial mediated formation of Fe-carbonate minerals under extreme acidic conditions. *Sci Rep* 4: doi:10.1038/srep04767.

Sánchez-Román M, Puente-Sánchez F, Parro V, *et al.* (2015) Nucleation of Fe-rich phosphates and carbonates on microbial cells and exopolymeric substances. *Front Microbiol* 6, doi:10.3389/fmicb.2015.01024.

Sand W, Gehrke T, Jozsa P-G, *et al.* (2001) (Bio)chemistry of bacterial leaching—direct vs. indirect bioleaching. *Hydrometallurgy* 59:159–175.

Siljeström S, Parenteau MN, Jahnke LL, *et al.* (2017) A comparative ToF-SIMS and GC–MS analysis of phototrophic communities collected from an alkaline silica-depositing hot spring. *Org Geochem* 109:14–30.

Sjövall P, Thiel V, Siljeström S, *et al.* (2008) Organic geochemical microanalysis by time-of-flight secondary ion mass spectrometry (ToF-SIMS). *Geostand Geoanal Res* 32:267–277.

Smith CA, O'Maille G, Want EJ, *et al.* (2005) METLIN: a metabolite mass spectral database. *Ther Drug Monit* 27:747–751.

Stoker CR, Cannon HN, Dunagan SE, *et al.* (2008) The 2005 MARTE robotic drilling experiment in Río Tinto, Spain: objectives, approach, and results of a simulated mission to search for life in the martian subsurface. *Astrobiology* 8:921–945.

Strohalm M, Kavan D, Novák P, *et al.* (2010) mMass 3: a cross-platform software environment for precise analysis of mass spectrometric data. *Anal Chem* 82:4648–4651.

Sutherland IW (2001) The biofilm matrix—an immobilized but dynamic microbial environment. *Trends Microbiol* 9:222–227.

Velasco F, Herrero JM, Suárez S, *et al.* (2013) Supergene features and evolution of gossans capping massive sulphide deposits in the Iberian Pyrite Belt. *Ore Geology Reviews* 53:181–203.

Westall F, Foucher F, Bost N, *et al.* (2015) Biosignatures on Mars: what, where, and how? Implications for the search for martian life. *Astrobiology* 15:998–1029.

Zhang L, Zheng P, He Y, *et al.* (2009) Performance of sulfate-dependent anaerobic ammonium oxidation. *Sci China B Chem* 52:86–92.

Address correspondence to:
David C Fernández-Remolar
SKL Lunar and Planetary Sciences
Macau University of Science and Technology
Avenida Wai Long
Taipa 999078
SAR China

E-mail: dcfremolar@must.edu.mo

Submitted 29 December 2020
Accepted 29 June 2021
Associate Editor: Victor Parro

Abbreviations Used

EDS = energy dispersive X-ray spectroscopy
EPS = extracellular polymeric substances
FAs = fatty acids
IPB = Iberian Pyrite Belt
MARTE = Mars Analog and Technology Experiment
SA = sulfate adducts
SEM = scanning electron microscope, scanning electron microscopy
ToF-SIMS = time-of-flight secondary ion mass spectrometer, time-of-flight secondary ion mass spectrometry